The carnosinase dipeptidase CNDP1 is a novel metabolic vulnerability in brain metastasis

Maria A. Gomez-Munoz[1, 2, #], Alcida Karz[1, 2, #], Maya Navarro[1, 2], Victoria Osorio-Vasquez[1, 2, 3], Olga Katsara[4], Adam Walker[5,8], Pietro Berico[1, 2], A. Paulina Medellin[9], Nicole M. Eskow[1, 2], Yunjing Wan[5], Milad Ibrahim[6], Somnath Tagore[10], Edridge K. D'Souza[10], Benjamin Izar[10], Eleazar Vega Saenz de Miera[6], Iman Osman[6], Michael Pacold[3], Xiangpeng Kong[7], Mitchell Levesque[11], Richard Possemato[1,3], Sheri L. Holmen[9], Robert J.Schneider[4], C. Theresa Vincent[4,12], Kelly V. Ruggles[5,8], Douglas E. Biancur[1, 3, *], Eva Hernando[1, 2,*].

Departments of [1]Pathology, [3]Radiation Oncology, [4]Microbiology, [5]Medicine, [6]Dermatology, [7]Biochemistry and Molecular Pharmacology, NYU Grossman School of Medicine, New York, NY 10016, United States

[2] Interdisciplinary Melanoma Cooperative Group, Perlmutter Cancer Center, NYU Langone Health, New York, NY, 10016, United States

[8] Institute of Systems Genetics, NYU Langone Health, New York, NY 10016, United States

[9] Huntsman Cancer Institute, University of Utah Health Sciences Center, Salt Lake City, UT 84112, USA; Department of Surgery, University of Utah Health Sciences Center, Salt Lake City, UT 84112, USA

[10] Herbert Irving Comprehensive Cancer Center, Columbia University, New York, NY 10032, United States

[11] University of Zurich, Switzerland

[12] Department of Laboratory Medicine, Karolinska Institute, 141 86 Stockholm, Sweden

 # these authors contributed equally

*corresponding author and lead contact: Eva Hernando (eva.hernando-monge@nyulangone.org)

*corresponding author: Douglas Biancur (Douglas.Biancur@nyulangone.org)

Abstract

Brain metastatic cells undergo metabolic adaptations, such as increased reliance on oxidative phosphorylation. Integrating proteomic and transcriptomic profiling of patient samples revealed a consistent upregulation of the carnosine dipeptidase-1 (CNDP1) in brain versus extracranial metastases. Carnosine is an abundant metabolite in brain and muscle, known to exert anti-proliferative effects on cancer cells. Here, we demonstrate that CNDP1 inhibition suppresses both the establishment and maintenance of melanoma brain metastasis while its ectopic expression is sufficient to confer brain metastatic potential to poorly metastatic cells. CNDP1 suppression results in activation of the Integrated Stress Response via Heme-Regulated Inhibitor Kinase and reprogrammed translation towards preferential expression of mitochondrial and survival transcripts. We further show that CNDP1 upregulation supports mitochondrial activity by limiting the levels of its substrate carnosine, a copper ionophore, thus protecting metastatic cells from carnosine-induced copper toxicity. Our studies reveal a novel metabolic adaptation during brain metastasis, which can be leveraged for therapeutic purposes.

Keywords: melanoma, brain metastasis, metabolic adaptation, mitochondria, metabolism, carnosinase, carnosine, ionophore, copper.

Introduction

While advances in cancer therapy have drastically improved patient care, metastatic disease is often refractory to current treatment options and remains the most common cause of cancer-related deaths(1,2). Primary tumor cells may acquire mutations or transcriptional programs that predispose cells to disseminate(3–5), and once they reach the metastatic niche, they must undergo further site-specific adaptations to survive in the new microenvironment (TME)(6–8). Understanding these adaptations is key to uncovering novel and targetable vulnerabilities of metastatic cells.

52 Specifically, brain metastases (BMs) are a major cause of cancer-related morbidity and
53 mortality, affecting nearly 40% of patients with advanced solid tumors, most frequently in patients
54 with carcinomas of the lung or breast (9–11), and melanoma(12). Despite tremendous advances
55 in surgical approaches, radiotherapy, and systemic targeted and immune therapies, patients with
56 symptomatic BMs experience reduced treatment response rates, even when extracranial
57 metastases (ECMs) are controlled(13–15). Therefore, there is an urgent need of improved
58 treatment options tailored to the unique BM biology(16–20).

59 Extensive efforts have been made to identify mechanisms of brain metastasis tropism (21–
60 25) . For instance, studies have shown that metastatic cells rewire their metabolism to adapt to
61 the distinctive properties of the brain such as higher oxygen concentration, distinct micronutrient
62 availability, amino acid deprivation or alternative sources of carbon(22,23,26,27). Genes involved
63 in oxidative phosphorylation have been found to be upregulated at both mRNA and protein levels
64 in melanoma brain metastasis (MBM) patient samples compared to extracranial
65 metastases(22,26), and patients with an increased oxidative phosphorylation signature in their
66 MBMs exhibit decreased survival(21,26). We have previously shown that melanoma cells derived
67 from the brain metastatic niche hold a higher oxidative potential than their extracranial
68 counterparts(25). Moreover, metastatic cells undergo metabolic adaptations that enhance their
69 capacity to survive under oxidative stress(28,29), such as modulating the expression of NADPH+
70 generating enzymes. Similarly, cells that metastasize to the leptomeninges are able to compete
71 for available iron with macrophages in the cerebrospinal fluid (CSF) by modulating lipocalin-2
72 expression in the hypoxic niche to support their metabolic needs, among other cellular
73 processes(30). A better understanding of metabolic dependencies in the brain metastatic niche
74 may reveal novel susceptibilities that can be exploited for therapeutic purposes.

75 Here, we integrated two datasets: mass spectrometry-based proteomics of melanoma
76 extracranial (non-brain metastasis; NBM) and MBM Short Term Cultures (STCs)(25), and
77 transcriptomics data from extracranial and brain metastasis samples(26), reasoning that gene

78 products consistently upregulated in MBM across different cohorts and two omics modalities
79 might have functional relevance to the MBM cascade. This integration revealed that expression
80 of the brain-associated dipeptidase CNDP1 is consistently increased in MBM versus NBM.
81 CNDP1, or carnosine dipeptidase-1, is a secreted peptidase known to cleave carnosine into its
82 component amino acids L-histidine and ß-alanine(31–34). Carnosine exerts a protective
83 physiological function in muscle, brain, liver and kidney, and is reported to have anti-glycation
84 effects and impact oxidative stress, though the respective underlying mechanisms, as well as
85 those governing its abundance, remain unclear(35–38). It has been recently suggested that these
86 properties of carnosine come from its ability to chelate metals such as copper and iron, which can
87 contribute to the formation of Advanced Glycation End (AGE) products through reactive carbonyl
88 or reactive oxygen species (ROS)(37–42). Carnosine administration *in vitro* is known to exert an
89 anti-proliferative effect on cell lines of various cancer types(34,43–45). We therefore hypothesized
90 that CNDP1 upregulation in MBM may provide an adaptative advantage to cancer cells in the
91 brain where abundant carnosine exhibits a tissue-protective role. Indeed, our work uncovers a
92 new role for CNDP1 in overcoming metabolic stress during MBM establishment by cleaving
93 carnosine excess and protecting cells from intracellular copper overload. Our studies reveal a
94 novel molecular mechanism of BM adaptation, and CNDP1 as a druggable vulnerability which
95 can be exploited therapeutically to prevent or treat BM.
96

97 **Results**

98 **Integrative multi-omics approach nominates CNDP1 as a driver of MBM**

99 To uncover mechanisms of adaptation to the brain microenvironment shared across
100 patients, proteomics data from paired NBM and MBM short-term cultures (STCs) (n=3 unique
101 patients) were compared to an RNA-sequencing (RNA-seq) dataset of 35 surgically resected
102 MBM and 41 NBM tissue specimens (n=29 unique patients, Table S1(25,26)). We compared
103 differentially expressed genes in paired MBM vs NBM samples to those found by proteomics

104 profiling (Figure 1A). By applying a cutoff of log2FC > 0.4 in both studies, and a p-value threshold
105 of 0.005 in the differential transcriptomic analysis, we compiled a list of candidate genes
106 upregulated in both cohorts, with Carnosine dipeptidase-1 (CNDP1) having the highest
107 upregulation on both datasets (Figure 1A, Table S2). CNDP1 is a secreted zinc metalloprotease
108 that cleaves the dipeptide carnosine into L-histidine and ß-alanine(46). *CNDP1* is predominantly
109 expressed in the mammalian brain and liver, while its homologue *CNDP2* and its counterpart in
110 carnosine metabolism *CARNS1* (carnosine synthase 1) are ubiquitously expressed (Figure S1A).
111 Data mining of SKCM TCGA (The Cancer Genome Atlas) transcriptomics data revealed that
112 *CNDP1* expression is significantly increased in metastatic (n=367) compared to primary samples
113 (n=104) (p=0.0054; Figure S1B). *CARNS1* levels were found increased and *CNDP2* levels
114 decreased during progression from primary to metastasis whereas CNDP1 increased in
115 metastatic (n=367) compared to primary samples (n=104) (p<0.006, p<0.001 and p<0.06,
116 respectively; Figure S1B). Neither *CNDP1* nor *CNDP2* transcript levels associate with melanoma
117 patients' overall survival in that dataset, while lower *CARNS1* correlates with shorter overall
118 survival in metastatic patients (p<0.002; Figure S1C). In a separate cohort, CNDP1 protein levels
119 within melanoma-infiltrated lymph nodes associate with shorter patient survival (n=59, p=0.03,
120 Figure 1B). Additionally, RNA-sequencing analysis of melanoma extended to resected lymph
121 nodes revealed higher expression of *CNDP1* in melanomas that metastasized to brain relative to
122 those that recurred to other sites (p=0.03, Figure 1C, Table S4). Single nucleus RNA-sequencing
123 (snRNA-seq) data from fresh-frozen patient samples(47) showed a higher percentage of MBM
124 cells expressing *CNDP1* compared to NBM (Figure 1D; $p = 6.22e^{-16}$). Extending our findings
125 beyond melanoma, analysis of lung and breast cancer transcriptomics datasets showed *CNDP1*
126 upregulation in BM samples relative to primary tissues (p<0.001; Figure 1E-F, S1D).
127 Immunohistochemistry analysis of a tissue microarray (TMA) of melanoma patient samples
128 confirmed higher CNDP1 levels in brain metastasis samples (n=70) compared to patient-matched
129 NBM (n=24), primary tumors (n=43) or healthy skin and cortex (p=0.02, Figure 1G, Table S3). We

130 confirmed the expression of CNDP1 by qPCR, immunoblotting and carnosinase activity in patient-
131 matched STCs (Figure S1D-F). Altogether, these data nominated CNDP1 as a potential driver of
132 brain metastasis.

133 Next, we investigated potential transcriptional programs driving *CNDP1* upregulation in
134 melanoma metastasis. *In silico* analysis of TCGA ATAC-seq data revealed open chromatin
135 regions in the *CNDP1* locus and identified an enhancer, the opening of which strongly correlates
136 with *CNDP1* expression (Fig. S1H-I). It has been reported that levels of *MITF*, the master regulator
137 of melanocyte expression (48), are significantly higher in BM versus NBM (47) , suggesting
138 *CNDP1* transcription could be driven by MITF. ChIPseq confirmed direct MITF binding to the
139 *CNDP1* promoter and enhancer (Fig. S1J), and MITF silencing resulted in decreased H3K27ac
140 at the *CNDP1* promoter and reduced *CNDP1* mRNA levels (Figure S1J-L). Together, our data
141 suggests that *CNDP1* expression may be at least partially governed by MITF.

142

143 **CNDP1 depletion and carnosine accumulation decrease *in vitro* proliferation of MBM**
144 **patient-derived short-term cultures**

145 To test the potential role of CNDP1 in MBM, we used a loss-of-function approach. CNDP1
146 silencing with two doxycycline (dox)-inducible shRNAs in two human MBM STCs (Figure 2A)
147 slowed cell proliferation after 24 h by G1 phase stalling ($p<0.001$, Figure 2B-C), suggesting that
148 CNDP1 is required for 2D cell growth in MBM cells. Importantly, 24 hours of dox-induced CNDP1
149 KD resulted in an increase in carnosine extracellular levels measured by ELISA (Figure S2A). We
150 then confirmed that carnosine supplementation at comparable concentrations to those found
151 physiologically in brain (49), leads to a proliferation defect in the same cells and increased
152 intracellular carnosine levels ($p<0.001$, Figure S2B-C). Additionally, CNDP1 dependency is not a
153 general feature of melanoma cells, as suggested by a proliferation assay in a non-brain tropic
154 melanoma cell line (Figure S2D). We confirmed the anti-proliferative effect of CNDP1 depletion
155 using RNA interference with pooled siRNA as an orthogonal approach ($p<0.001$; Figure 2D-E).

156 Taken together, these data suggest cellular reprogramming to the brain microenvironment
157 involves CNDP1 induction, exposing a novel and potentially targetable vulnerability of brain
158 metastases.
159
160 **CNDP1 inhibition suppresses brain metastasis establishment and maintenance in**
161 **xenografts, and Cndp1 ectopic expression confers brain tropism to syngeneic models**
162 To test if CNDP1 is required for BM establishment and/or growth *in vivo*, NSG mice were
163 injected intracardially with patient-derived 12-273 BM cells stably transduced with either CNDP1-
164 targeting or non-targeting control shRNA (Figure 3A-H). *In vivo* experiments were carried out
165 using two approaches: i) constitutive CNDP1 knockdown, in which dox-containing chow was
166 administered to mice right before tumor cell injection (Figure 3A-D), which addresses the
167 requirement of CNDP1 for the *establishment* of metastasis, and ii) a more therapeutically relevant
168 approach in which dox was administered after metastases were seeded, which assesses if
169 CNDP1 is required for metastasis *maintenance* and growth (Figure 3E-H). Mice were humanely
170 euthanized when any group started to show symptoms of distress or more than 20% weight loss,
171 and organs were collected and processed for histological analyses. To quantify metastasis
172 burden, we used both whole body bioluminescence live imaging (BLI) and MetFinder(50), a
173 machine learning-powered tool we developed to segment, measure and quantify metastases in
174 H&E-stained sections of murine tissues at termination. Our data shows strongly reduced brain
175 and liver metastatic burden upon CNDP1 silencing with both shRNA ($p<0.03$, n.s. for shCNDP1-
176 1 in the inducible approach in liver; Fig. 3D,H) A similar phenotype was observed in another
177 patient-derived model, 10-230 BM, and in a brain-tropic breast cancer model (MDA-231 Brm2),
178 after either constitutive (Fig S3A-D) or inducible CNDP1 knock-down (Fig S3E-L), supporting a
179 role for this dipeptidase across cancer types. RNA-seq of GFP positive cells sorted from
180 metastatic lesions confirmed that *CNDP1* silencing was maintained *in vivo* (Fig. S3M).

181 Next, we tested whether CNDP1 ectopic expression is sufficient to enhance BM
182 development. Murine Yumm3.2 melanoma cells (Braf$^{V600E/wt}$ Cdkn2a-/- Pten-/-(51–53)), which do
183 not metastasize when injected subcutaneously in C57BL/6J mice, were stably transduced with
184 lentiviral vectors carrying HA-tagged Cndp1 or Akt1-E17K, which was previously shown to
185 enhance metastasis development in this model(52) (Figure 3I). Cndp1 expression is not detected
186 in these murine melanoma cells (not shown). Ectopically expressed Cndp1 exhibits carnosinase
187 activity and confers a proliferation advantage *in vitro* ($p<0.01$, Figure S2E-G). Control, Akt1-E17K-
188 and Cndp1-HA-transduced Yumm3.2 cells were subcutaneously injected in C57BL/6 mice. Upon
189 reaching the maximum tumor volume, mice were euthanized, and organs harvested and
190 examined by ex-vivo BLI for metastasis burden (Figure 3J-K). We observed that Cndp1-HA
191 expressing cells gained exclusive brain tropism, with a higher incidence than Akt1-E17K
192 transduced cells (62% vs 0 % (parental) vs 40% (Akt-E17K), $p<0.001$), which were also able to
193 form lung and liver metastasis (Figure 3J-K). All these data points to a specific role for CNDP1 in
194 enhancing BM development.
195 Our results support a role for CNDP1 in brain metastasis and expose CNDP1 targeting as
196 a promising therapeutic intervention against these tumors. Interestingly, the observation that
197 single nucleotide polymorphisms (SNPs) impairing CNDP1 secretion protect diabetic patients
198 from developing nephropathy (36,54) has sparked interest in developing CNDP1 inhibitors, some
199 of which have shown promising activity in preclinical models(55). Our studies provide a rationale
200 for further developing small molecule compounds or antibodies targeting CNDP1.
201
202 **CNDP1 knockdown elicits an Integrated Stress Response and translational**
203 **reprogramming**
204 To further characterize the role of CNDP1 to tumor progression, we employed an unbiased
205 approach integrating LC/MS metabolomics and bulk RNA-seq of shCNDP1-transduced cells
206 induced with doxycycline for 72h (Figure 4A, Tables S5,6). We analyzed the resulting data with

207 the MetaboAnalyst algorithm(56) (Table S7), which uses hypergeometric tests to identify
208 enrichment of both transcript-based and mass spectra-based data in metabolic pathways. We
209 found that “Aminoacyl tRNA-synthesis” was the most deregulated metabolic pathway in tumor
210 cells upon CNDP1 suppression (Figure 4B, Table S7). To examine if these changes in tRNA
211 synthesis may have implications for translation, we performed additional MS/MS (proteomics)
212 analysis of 10-230 BM cells transduced with indicated shRNA (Table S8) and integrated these
213 data with LC/MS (metabolomics) data (Table S5). This analysis revealed an accumulation of
214 amino acids such as phenyl-alanine, arginine, tyrosine and leucine together with their respective
215 aminoacyl tRNA-synthetases (Figure 4C) upon CNDP1 silencing.

216 Further elucidating the cellular adaptative response triggered by CNDP1 silencing,
217 transcriptomic and proteomics profiling revealed changes in translation initiation, elongation and
218 RNA metabolism along with stress response pathways (Figures 4D, S4A, Tables S6,S9-10).
219 Together, these changes were reminiscent of activation of the Integrated Stress Response (ISR),
220 a cellular mechanism that halts or rewires protein synthesis in response to various sources of
221 stress.(57) Indeed, we observed an increase in expression of ATF4 targets (Figure 4E,F) and p-
222 Ser51-eIF2α levels (Figures 4G, S4B), both hallmarks of ISR activation, upon CNDP1 depletion.
223 Moreover, a p-eIF2α inhibitor, ISRIB,(58) was able to partially rescue the proliferation defect
224 induced by CNDP1 knock-down ($p<0.02$) (Figure 4H).

225 Although activation of the ISR often leads to a general shutdown of translation, CNDP1
226 silencing only had a modest impact on overall translation, in comparison to treatment with
227 cycloheximide (CHX), a *bona fide* translation inhibitor(59) (Figure 5A). CNDP1 KD cells showed
228 decreased mTOR activity, as revealed by p70 pS6K1, p-4E-BP1 and p-eIF4E levels, key
229 modulators of translation initiation(60,61) (Figure 5B). mTOR modulation has been previously
230 observed in response to TCA perturbation, such as a decrease in α-Ketoglutarate or changes in
231 branched chain amino acid (BCAA) metabolism including isoleucine, leucine and valine, as

232 observed upon CNDP1 KD (Figure 4B,C, Tables S5(62,63)). Additionally, transcriptomic data
233 analysis of human melanoma metastases (i.e., TCGA, including various metastatic sites;
234 GSE185386, including only MBM), revealed that *CNDP1* expression anti-correlates with
235 translation and stress response gene signatures (Figure 5C). Our data pointed to a selective
236 reprogramming of translation initiation rather than a complete shut down upon CNDP1 KD. To
237 better understand specific translation changes elicited by CNDP1 KD, we performed polysome
238 isolation followed by RNA-seq. Polysome profiling revealed changes in translation of mRNAs
239 directly involved in mitochondria, ribosomes and cell division genes (Figure 5D-E, Figure S5A-B,
240 Table S11). Concomitantly, we observed changes in eIF3d expression, suggestive of a shift from
241 canonical to non-canonical cap-dependent translation possibly mediated by eIF3d/DAP5 (Figure
242 S5C). It has been shown that eIF3d promotes selective cap-dependent translation of mRNAs
243 involved in cell survival, such as mitochondrial genes (64,65). Of note, human BM cells expressing
244 CNDP1^{high} levels are significantly enriched in mitochondrial genes in comparison to CNDP1^{low}
245 cells (Table S12). Altogether, these data suggest that CNDP1 silencing initiates the ISR which
246 reprograms the translation machinery to support mitochondrial respiration and cell cycle related
247 transcripts.
248
249 **CNDP1 depletion perturbs mitochondrial activity and results in increased intracellular**
250 **copper levels**
251 We next sought to understand how CNDP1 KD triggers mitochondrial stress, resulting in
252 activation of the ISR and translation rewiring. Given our data indicating a shift towards translation
253 of mitochondrial transcripts, we focused our attention on the mitochondria. Indeed, we observed
254 profound morphological changes in the mitochondria of CNDP1 KD cells, including a smaller
255 number of cristae per mitochondria (Figure 6A-E, Figure S6A-E), a phenotype previously reported
256 as functionally defective(66). *In vivo*, we observed reduced expression of the mitochondrial
257 transport protein Tom20 in brain metastases upon acute CNDP1 KD (Figure 6F), which is

258 indicative of dysfunctional mitochondrial structures (67). Taken together, these data raised the
259 possibility that carnosine accumulation from CNDP1 inhibition causes mitochondrial dysfunction.
260 Consistent with this hypothesis, both CNDP1 KD and carnosine treatment elicited a significant
261 decrease in oxygen consumption rate (OCR) measured by Seahorse assays (Figure 6G, Figure
262 S6F, $p<0.02$).

263 These findings led us to investigate if CNDP1 modulation also impacts Gln usage in the
264 TCA cycle of melanoma cells. We performed Gln tracing experiments by using U-^{13} C5 labelled
265 Gln and traced its incorporation by GC/MS analysis(68) in melanoma brain metastasis derived
266 cells transduced with shRNA targeting CNDP1 as indicated (Figure 6H). We found that after 24h
267 of silencing, CNDP1 KD cells display significantly reduced glutamine usage as evidenced by the
268 lower levels of its glutamine-derived metabolites in the tricarboxylic acid (TCA) cycle: α-
269 Ketoglutarate (M+5), Fumarate, Malate and Citrate (M+4) (Figure 6I). All these effects were
270 mimicked by carnosine addition (Figure S6G-H). These data demonstrate that both CNDP1 KD
271 and carnosine treatment impact TCA cycle activity. In addition to mitochondrial dysfunction,
272 CNDP1 KD cells accumulated ROS, as indicated by CellROX measurements (Fig. 6J).
273 Concomitant with ROS accumulation we observed the activation of heme-regulated inhibitor (HRI)
274 kinase (Figure 6K), likely responsible for the above mentioned ISR activation (Figure 4).

275 Having observed that CNDP1 silencing impairs mitochondrial respiration and results in
276 ROS accumulation, translation stalling and reprogramming, we looked for potential mechanisms
277 directly triggering these effects downstream of CNDP1. Carnosine has been reported to work both
278 as an ion chelator and ionophore, that is, able to transport iron and copper into the intracellular
279 space.(69) We hypothesized that carnosine accumulation upon CNDP1 KD could lead to
280 increased intracellular copper uptake through SLC transporters(70) and result in copper overload.
281 Intriguingly, we observed CNDP1 KD cells exhibit dysregulation of genes involved in heavy metal
282 metabolism such as iron (*LCN2, HMOX*) and copper transporters (*SLC46A3, ATP7B*) (Figure S6I-
283 K). Indeed, by analyzing scRNA-seq data of MBM,(22) we found a significant enrichment in genes

284 controlling copper homeostasis in CNDP1^{high} vs CNDP1^{low} MBM cells (Figure S6L). By staining
285 cells with a permeable fluorescent dye (CS1) that binds free intracellular copper, we measured
286 copper levels in CNDP1 KD and carnosine-treated cells along with cells treated with an
287 established copper ionophore, Elesclomol(71), as a positive control. Indeed, both CNDP1 KD and
288 carnosine-treated cells contain significantly higher intracellular copper levels, comparable to
289 those of cells treated with Elesclomol ($p<0.05$ or indicated, Figure 6L). Copper mediated toxicity
290 also affects the lipoylation of TCA enzymes such as Pyruvate dehydrogenase (PDH) and 2-
291 oxoglutarate dehydrogenase (OGDH)(72), that results in degradation of these enzymes (Figure
292 S6M), and Fe-S clusters assembly(73), leading to a decrease of both glutamine usage and
293 OXPHOS dependent metabolism. Additionally, copper overload has been described to cause
294 ROS accumulation(74). Therefore, intracellular copper overload in CNDP1 KD and carnosine-
295 treated cells could explain the previously observed phenotypes of mitochondrial dysfunction and
296 accumulation of ROS (Figure 6G-J, S6F,G).

297 Altogether, our studies support CNDP1 upregulation as a metabolic adaptation of cancer
298 cells that increases their fitness during BM, likely by overcoming copper toxicity induced by
299 carnosine accumulation in the brain metastatic niche (see model in **Figure S7**). CNDP1 inhibition
300 emerges as a plausible strategy against metastatic progression by inducing metabolic stress.

301

302 **Discussion**

303 Understanding distinct biological features of site-specific metastatic adaptation offers the
304 possibility of discovering new targets and therapeutic options. In this study, we integrate two data
305 sets, RNA-seq and proteomics,(25,26) comparing BM versus extracranial tumor samples to
306 identify potential genes relevant to BM establishment and development. This analysis nominated
307 a secreted dipeptidase, carnosine dipeptidase 1 or CNDP1, as a plausible player in melanoma
308 brain metastasis. We also found *CNDP1* upregulated in lung and breast cancer brain metastases
309 versus primary tumors across multiple databases. Silencing CNDP1 slows proliferation *in vitro* of

310 brain metastasis-derived short-term cultures and impairs BM establishment and maintenance. A
311 defect in liver metastasis upon CNDP1 silencing was also observed in our brain-tropic xenograft
312 models; not surprisingly, since intracardiac injection favors hematogenous spread which allows
313 our brain metastasis derived cells to yield not only brain but also liver metastases[25,116]. Moreover,
314 carnosine is abundant in the liver[3], thus CNDP1 upregulation may also provide a growth
315 advantage there. However, Cndp1 ectopic expression exclusively conferred brain tropism to non-
316 metastatic syngeneic models, supporting CNDP1 as a brain metastasis driver. In all, we
317 demonstrate that high CNDP1 levels confer cancer cells increased ability to seed and colonize
318 the brain. While CNDP1 target, carnosine, has been studied for its various chemical properties,
319 the contribution of CNDP1 to human disease and in particular cancer is understudied. A mutant
320 form of this dipeptidase was found associated with less severe nephropathy in type II diabetes
321 patients(36,54); however, our study is the first to demonstrate the contribution of CNDP1 to brain
322 metastasis.

323 Whether CNDP1 expression is induced once cells arrive to the brain, or if CNDP1^{high} cells
324 have increased ability to seed in the brain parenchyma is unclear. In support of the latter, we
325 found higher *CNDP1* levels in lymph nodes of melanoma patients that went on to develop brain
326 metastases than in those that did not have BM. In melanoma, recent studies have shown cells
327 can adopt different cell states, characterized by distinct transcriptional programs associated with
328 varying metastatic potential(75,76). We did not find the expression of CNDP1 to be associated
329 with specific transcriptional states (data not shown), yet we observed a plausible regulation of
330 CNDP1 by MITF. Indeed, in Biermann et al., we reported an enrichment of the MITF signature in
331 MBM vs extracranial metastasis.(22) However, our preliminary data suggest *CNDP1* upregulation
332 in BM across non-melanoma tumors (i.e., breast and lung adenocarcinoma BM), likely by MITF-
333 independent pathways. Further studies will be necessary to dissect CNDP1 regulation, and
334 whether CNDP1^{high} cells can be detected in primary tumors and perhaps even hold prognostic
335 value.

336 In this study, we propose that melanoma BM cells overcome carnosine-mediated copper
337 overload in the metastatic niche by upregulating CNDP1. Copper uptake has been reported to
338 enhance MAPK signaling in BRAFV600E mutant cells, and trigger MAPK inhibitor (MAPKi)
339 resistance in melanoma cells(77). It also known how OXPHOS activation depends on MAPK
340 signaling(78,79) . We therefore hypothesize that melanoma cells that resist copper overload may
341 be able to not only escape from MAPKi treatment, but also to survive in the BM niche. By
342 DepMap(80) data mining we found that $MITF^{high}$ melanoma cell lines are more resistant to
343 Elesclomol treatment (Figure S6N). Moreover, melanocytic-like ($MITF^{high}$) cells may exhibit more
344 tropism for BM(22) because of their well-known copper dependency, which these cells utilize for
345 tyrosinase activity and melanin production(81–83) .
346 Our results reveal a detrimental effect of CNDP1 silencing in the establishment and
347 maintenance of metastasis *in vivo* along with a mild effect on proliferation *in vitro* in our brain-
348 derived models. The main reported substrate of CNDP1, carnosine, is known to be abundant in
349 brain (e.g., 3 mg / 100 gr of tissue in rat brain), where it is produced mainly by oligodendrocytes
350 and displays antioxidant, scavenging, pH buffering and anti-neuroinflammatory properties(38,41–
351 43) . Carnosine has been studied as a dietary supplement in its native form, as well as in forms
352 less easily cleaved by CNDP1, such as N-acetyl carnosine and zinc-L-Carnosine(34) . Small
353 randomized controlled trials have shown that carnosine supplementation can benefit the short-
354 term memory of healthy elderly patients, as well as those with Mild Cognitive Impairment(84,85).
355 Our studies support previous evidence of carnosine's ability to function as a copper ionophore(39)
356 as part of a number of mechanisms that regulate tightly the distribution and transport of this
357 micronutrient. These findings open a new avenue in the study of carnosine in copper-dependent
358 mechanisms such as hepatic function or dopamine production and their potential effects in other
359 diseases(81,82,86). For instance, highly abundant oligodendrocytes in the substantia
360 nigra(87,88), that express both CARNS1 and CNDP1(49), may contribute to control carnosine-
361 mediated copper uptake by dopaminergic neurons used for dopamine production. Meanwhile,

362 carnosine supplementation has been reported to exert anti-proliferative effects on tumor cells(44).
363 In highly glycolytic tumors, it has been reported that Isoform 2 of CARNS1 (CARNS2) controls
364 carnosine levels, which have immunomodulatory effects during hepatic cancer progression(89).
365 We hypothesized that carnosine accumulation could be detrimental to tumor growth, and that
366 metastatic cells may benefit from cleaving carnosine and mitigating its antitumoral effects. The
367 regulation of carnosine levels in tissues is an open question; for instance, humans are known to
368 have higher levels of circulating CNDP1 in serum than other mammals(31,33). In fact, higher apes
369 and the Syrian hamster have evolved an export signal sequence at the *CNDP1* locus, absent
370 from other species, for unclear reasons(32,34). Carnostatine is a structural analog of carnosine
371 that has been described to inhibit CNDP1 dipeptidase activity in preclinical models of diabetic
372 nephropathy[52]. Future *in vivo* studies could test the therapeutic potential of pharmacological
373 inhibitors of CNDP1 able to cross the blood brain barrier, alone or in combination with approved
374 therapies.

375 CNDP1 is also known to cleave homocarnosine, a dipeptide made of GABA and L-
376 histidine that exists at higher concentrations in the human than in the mouse brain(37,90,91).
377 GABA is an inhibitory neuromodulator mainly produced in the cytosol of GABAergic neurons that
378 regulates the activity of astrocytes and oligodendrocytes(92–94). We and others have reported
379 that brain metastatic tumors can modulate the activity of neural cells in the metastatic niche by
380 various mechanisms(25,95). In addition, GABA release from melanocytes has been shown to
381 promote melanoma initiation by influencing their crosstalk with keratinocytes(96). Future studies
382 could determine if increased GABA —from CNDP1-mediated homocarnosine cleavage — allows
383 metastatic cells to hijack the neural microenvironment to their advantage.

384 To our knowledge, we are the first to report that CNDP1 silencing elicits translation
385 reprogramming by modulating two interconnected pathways, ISR and mTOR, known to respond
386 to various sources of cellular stress(61,97–100). ISR activation and mTOR inhibition upon CNDP1
387 KD result in preferred translation of mitochondrial and survival proteins, most likely controlled by

388 eIF3d cap-dependent translation mechanisms(64,65), as previously shown under other forms of
389 cellular stress. Extensive efforts have tried to determine if ISR activation is a barrier or conduit for
390 tumor progression(29,99,101,102). ISR activation in response to CNDP1 KD leads to changes in
391 the total AA pool, accumulation of tRNAs, and preferential translation of survival factors without
392 inducing cell death. Genetic inhibition of CNDP1 significantly reduces brain metastasis burden;
393 however, ISR activation upon CNDP1 KD could eventually allow cell survival in the metastatic
394 niche. These adapted cells might be able to persist, acquiring additional changes that may permit
395 tumor recurrence.

396 The shift of the translation machinery towards mitochondria-related transcripts paralleling
397 copper accumulation upon CNDP1 KD particularly captured our attention. Whereas iron
398 homeostasis is tightly post-transcriptionally regulated by Iron Response Elements (IREs)(103)
399 and Iron Regulatory Proteins (IRPs)(103,104), similar mechanisms regulating copper metabolism
400 have not yet been identified in human models(105–107). As discussed above, mitochondrial
401 metabolism has been shown to play a key role in the establishment of brain metastasis (22,25,26).
402 Proper oxidative phosphorylation relies on various factors,(21,22,26) including metal transport, a
403 key limiting process that links mitochondrial function and ROS homeostasis(108). Recent studies
404 have shown that cancer cells develop different adaptative mechanisms aimed at collecting heavy
405 metals from the metastatic niche to support their metabolic function(109,110). Their reliance on
406 heavy metals and particularly copper uptake becomes a vulnerability for brain metastatic cells.
407 As such, upon CNDP1 silencing, accumulation of the ionophore carnosine (39,40) may induce
408 copper toxicity(72,74,111) and mitochondrial malfunction. Supporting this model, CNDP1
409 depletion recapitulates the reported phenotypic effects of copper overload including ROS
410 accumulation(40,74,112), reduced OCR(73) and degradation of lipoylated TCA
411 enzymes(72,111).

412 Our work exposes the relevance of copper transport and uncovers a mechanism
413 underlying oxidative phosphorylation reliance as a key metabolic adaptation to the brain

414 metastatic niche. We found the dipeptidase CNDP1 tipping the balance of complex, interrelated
415 mechanisms of cell survival emerging under metabolically demanding circumstances. Future
416 studies will reveal how to further exploit these cell vulnerabilities to maximize the therapeutic
417 potential of CNDP1 pharmacological inhibitors, alone or in combination with approved therapies.
418

419 **Methods**

420 **Patient samples**

421 Patients' tumor samples from infiltrated lymph nodes were collected from melanoma
422 patients who were prospectively enrolled in the Interdisciplinary Melanoma Cooperative Group
423 Database (IMCG) at NYU Langone Health (IRB #10362). Inclusion criteria for this
424 clinicopathological database included patients who presented to the Laura and Isaac Perlmutter
425 Cancer Center (2002-2018) for melanoma and were accrued within two months of diagnosis. All
426 patients signed NYU Langone Health Institutional Review board-approved consent to allow using
427 their specimens for research and to conduct follow-up.

428 Tissue microarray samples were acquired by agreement with Dr. Levesque lab from
429 University of Zurich. All patients included in this study have signed a patient release form, which
430 has been approved by an ethics committee and assigned the numbers EK647 and EK800.
431

432 **Data mining**

433 *TCGA.* Data from The Cancer Genome Atlas Skin Cutaneous Melanoma Firehose Legacy
434 dataset (n = 472 samples, The Cancer Genome Atlas (RRID:SCR_003193) was analyzed using
435 cBioPortal (RRID:SCR_014555), (113)), which reports RNA-sequencing data in RSEM. Survival
436 analysis based on gene expression in the TCGA cohort was carried out using TIMER
437 (RRID:SCR_018737, (114)), the Tumor Immune Estimation Resource, which draws Kaplan-Meier
438 curves based on a user-defined cutoff of expression by percentage compared to the median, and
439 reports p values based on log-rank testing. Primary and metastatic samples were analyzed
440 separately.

441 *Analysis of scRNA-seq data.* Integration of samples from *Biermann et al. (22)* was carried
442 out using Seurat's CCA function (RRID:SCR_007322) in R studio (R Project for Statistical
443 Computing (RRID:SCR_001905) and Bioconductor (RRID:SCR_006442). Tumor cells were
444 parsed from non-tumor cells: non-tumor cells were excluded based on expression of genes
445 unique to immune and stromal populations (using AddModuleScore and AUCell function
446 (RRID:SCR_021327)). Next, malignant cells were segregated in *CNDP1* high and low using SCT
447 (Single Cell Transform) (expression > 0 as threshold to plot a copper signature ((115)WP3286,
448 WikiPathways (RRID:SCR_002134)) in *CNDP1*-high vs -low cells. CNDP1 expression from Non-
449 Small Cell Lung Cancer primary and brain metastasis was obtained as described in *Tagore,*
450 *Caprio et al.* in press in Nature Medicine.

451 *Other databases.* Raw, normalized or analyzed data were downloaded from Gene
452 Expression Omnibus (GEO) (RRID:SCR_005012) following each study's directions and code
453 indicated in figure legends. Statistical analysis as described in figure legends.

454 *TCGA-ATACseq.* Normalized ATACseq counts from 370 TCGA patients were retrieved
455 from UCSC Xena Browser database (RRID:SCR_018938). 10kb BIN segments around the
456 *CNDP1* and *CNDP2* loci were visualized by heatmap using Prism10 (RRID:SCR_002798) and
457 averaged for the ATACseq counts. Next, ATACseq counts in 10kb BIN segments around *CNDP1*
458 promoters were averaged and plot against matched RSEM expression counts for Pearson's
459 correlation using Prism10 (RRID:SCR_002798).

460 *GTEx, Genotype-Tissue Expression*. We utilized Genotype-Tissue Expression
461 (RRID:SCR_013042) data to assess expression from various tissues to identify tissue-specific
462 and cross-tissue expression patterns of *CNDP1, CNDP2* and *CARNS*1. The data used for the
463 analyses described in this manuscript were obtained from the GTEx Portal on 08/11/2023.

464 *Depmap.* Gene expression data for *MITF* was obtained from the "DepMap Public 22Q2"
465 (Cancer Dependency Map Portal (RRID:SCR_017655)(80)) release, which includes RNA-seq
466 data (TPM, transcripts per million) for melanoma cell lines. *MITF* expression data was filtered to

467 retain melanoma-derived cell lines only by cross-referencing with metadata on cell line origin. For
468 each melanoma cell line, the area under the dose-response curve (AUC) was extracted as a
469 measure of Elesclomol sensitivity, with lower AUC values indicating higher sensitivity to the drug.
470 Correlation was calculated using Pearson's correlation coefficient.
471

472 **Plasmid generation**

473 CMV-Luciferase-EF1α-copGFP (GFP-Luc) Lentivector Plasmid was purchased from BD
474 Biosciences (BLIV511PA-1). Tet-pLKO-puro was purchased from Addgene
475 (RRID:Addgene_98398). shRNAs were cloned as previously described 115) into Tet- pLKO-puro
476 using AgeI (NEB, Cat#R3552S) and EcoRI (Thermo, Cat#FD0275) restriction sites. pLKO tet-on
477 scrambled non-targeting control (shNTC) was purchased from Addgene
478 (RRID:Addgene_47541).

479 The FG12-HA-AKT1^{E17K} Luciferase-IRES-eGFP lentiviral vector has been described(52).
480 Cndp1-HA cDNA was synthesized by Gene Universal in the pENTR2B plasmid. Gateway cloning
481 was used to recombine the pENTR2B-Cndp1-HA entry clone and the pDEST FG12-Luciferase-
482 IRES-eGFP lentiviral destination vector (synthesized in Gene Universal) to generate the lentiviral
483 vector FG12-Cndp1-HA- Luciferase-IRES-eGFP.
484

485 **siRNA pools and transfection**

486 NON-targeting control (NTC) plus Human siRNA pools, ON-TARGET plus *CNDP1* and
487 *MITF* siRNAs were purchased from Dharmacon (QTE-3158440G, L-005824-00-0005, L-008674-
488 00-0005). 150,000 to 200,000 melanoma cells were seeded in 6-well plates and transfected with
489 20μM siRNA pools using Lipofectamine 2000 (Invitrogen,Cat#11668019) following
490 manufacturer's recommendations.
491

492 **Lentivirus production and infection**

493 HEK293T (RRID:CVCL_0063) cells at 80% confluency were co-transfected with 12 µg of
494 lentiviral expression constructs, 8 µg of psPAX2 (RRID: Addgene_12260) and 4 µg pMD2.G
495 (RRID: Addgene_ 12259) vectors using Lipofectamine 2000 (Invitrogen, Cat#11668019) following
496 manufacturer's recommendations for Tet-pLKO-puro system. Packaging plasmids psPAX2 and
497 pCMV-VSV-G (RRID: Addgene_8454) were used in combination with FG12-HA-AKT1-Ei7K
498 Luciferase-IRES-eGFP (52,117) to generate virus for stable cell line generation as described
499 below. At 48h and 72h post transfection, supernatants were collected, filtered (0.45 µm) and
500 stored at −80°C. Melanoma cells were infected with lentiviral supernatants supplemented with
501 polybrene (EMD Millipore, Cat#TR-1003-G) at a final concentration of 4µg/mL. Twenty-four hours
502 after infection, cells were selected by cell sorting by GFP fluorescence for GFP-Luc transduced
503 cells or treatment with puromycin (1 ug/mL, Thermo Fisher Scientific, Cat #A1113803), blasticidin
504 (10 ug/mL, Invivogen, Cat#ant-bl-1) or hygromycin (300 ug/mL, Thermo, Cat#10687010)
505 accordingly.

506 **Cell culture**

507 Melanoma short-term cultures (STCs) were derived as described and used at passage
508 (25,51,118). For maintenance cultures, STC cells were grown in DMEM (Corning, Cat #10-013-
509 CM) with 10% fetal bovine serum (regular: Corning, Cat#35-010-CV, Tet-free: Neuromics,
510 Cat#FBS002-T), 1 mM Sodium Pyruvate (Cytiva, Cat#SH30239.01), 4 mM L- Glutamine (Sigma-
511 Aldrich, Cat #59202C), 25 mM D-Glucose (Gibco, Cat#A2494001), 1% Nonessential Amino Acids
512 (Sigma-Aldrich, Cat#M7145-100ML), 100 units/mL penicillin, and 100 ug/mL streptomycin (Gibco,
513 Cat# 15-140-163). For functional assays, cells were seeded in DMEM (Corning, Cat #10-013-
514 CM) with 10% dialyzed Tet-free fetal bovine serum (Neuromics, Cat#FBS002-T), 4 mM L-
515 Glutamine (Sigma-Aldrich, Cat #59202C) and 25 mM D-Glucose (Gibco, Cat#A2494001).

516 HEK293T cells (RRID:CVCL_0063), MDA-231-Brm2 (RRID:CVCL_VR36) and SKMEL-239 (
517 RRID:CVCL_6122) melanoma cells(119) were grown in DMEM (Corning, Cat #10-013-CM)with
518 10% fetal bovine serum (FBS, Corning, Cat#35-010-CV), 1 mM Sodium Pyruvate (Cytiva,
519 Cat#SH30239.01), 4 mM L-Glutamine (Sigma-Aldrich, Cat #59202C), 25 mM D-Glucose (Gibco,
520 Cat#A2494001), 100 units/mL penicillin, and 100 ug/mL streptomycin(Gibco, Cat# 15-140-163).
521 YUMM3.2 cells were grown in F12/DMEM media (Thermo Fisher) supplemented with 10% FBS, 1
522 µg/mL penicillin-streptomycin (Thermo Fisher), and 1 µg/mL NEAA (Thermo Fisher). Cell lines
523 were maintained in a 5% CO2 incubator at 37°C and were routinely tested for Mycoplasma
524 contamination by using ATCC Kit (30-1012K) following manufacturer instructions.

525

526 **In vitro proliferation assay**

527 3,500 to 4,000 cells per well were seeded in 96 wells and monitored for 72 to 96 hours.
528 Cells transduced with Tet-pLKO-puro shRNAs were treated with doxycycline 1 ug/mL (Goldbio,
529 Cat #24390-14-5) for at least 48 hours before seeding or with indicated treatment.

530 *Incucyte*. After allowing cells to adhere overnight, Incucyte Software V2022.1, 2022.2, and
531 2023.1 (Sartorius IncuCyte SX5 Live Cell Analysis System (RRID:SCR_026298)), were used to
532 capture brightfield whole-well images. Masks for delineating confluence were manually adjusted
533 to ensure only live cells were captured, such as a minimum of 100 μM size per object. Images
534 were taken and analyzed every 6-12 hrs. Percent confluency was normalized to time=0 reading
535 to obtain a fold change value.

536 *Crystal violet staining.* After allowing cells to adhere overnight, a baseline plate was
537 obtained by removal of media and fixation in 0.1% glutaraldehyde for 15 minutes, then stored with
538 PBS(Corning, Cat #21-031-CM) in each well at 4C. Remaining plates were fixed every 24 hours
539 thereafter and/or at the experimental endpoint. Wells were stained with 0.5% crystal violet in PBS
540 for one hour and washed extensively with water. Crystal violet retained by cells was then eluted

541 by incubation in 250 μL 15% acetic acid for 1 hour with shaking, and absorbance at 590 nm was
542 measured. Absorbances were normalized to the absorbances from the baseline plate to obtain a
543 fold change value.
544
545 **Cell cycle analysis**
546 Cell cycle analysis was carried out using the Click iT EdU kit (Thermo Fischer, Cat
547 #C10636) to approximate DNA replication, and FxCycle Far Red (Thermo Fischer, Cat #F10348)
548 to measure total DNA content. Briefly, STC cells expressing control or CNDP1-targeting Tet-On
549 shRNA's were plated at 250,000 cells per well in 6-well plates with 1 ug/mL doxycycline. An
550 additional dose of doxycycline was added at 48 h post plating. At 72h post-plating, cells were
551 incubated with 10 μM EdU for 4 h. Then, cells were collected by trypsinization, washed in 3 mL
552 3% BSA in PBS, spun at 1200 rpm for 4 mins, fixed in 250μL Fixation buffer (Biolegend, Cat#
553 420801) for 20 mins in the dark at room temperature, washed in 3 mL 3% BSA, spun again.
554 Permeabilization and Click-iT reaction were executed according to kit instructions, followed by
555 FxCycle Far Red staining and analysis on BD LSR II Flow Cytometer.
556
557 **In vitro treatments**
558 Crystalline >99% L-carnosine (Sigma-Aldrich, Cat #C9625-25G) was dissolved into Media
559 or PBS (see Cell Culture) at a concentration of 200 mM by rocking in a light-protected 50 mL
560 conical tube. Solutions were pH adjusted to match base Media by adding HCl dropwise (~pH
561 7.45), then filtered using a 0.2 µm filter. Stocks were light-protected and maintained at -20C until
562 use, when they were thawed at room temperature and diluted into media. Cells were treated in a
563 10 μM to 50 mM range. ISRIB (phospho-eIF2a inhibitor, Selleck Chemicals, Cat#S7400) was
564 diluted in DMSO at 1mM stock solution and added *in vitro* at 1 μM final concentration for 72 hours.

565 Elesclomol (Selleck Chemicals, Cat#S1052) was diluted in DMSO 10 mM and added *in vitro* in a
566 range of 10 nM to 50 μM for 24 hours.
567
568 **L-Histidine assay**

569 Carnosinase activity was analyzed by measuring liberated L-histidine using a protocol
570 adapted from Teufel et al 2003(33). Briefly, conditioned media was collected, centrifuged to
571 remove dead cells and debris, and supernatant isolated. Adherent cells were rinsed in PBS and
572 scraped, and pellets were lysed in 50 mM Tris pH 8 with protease inhibitor (Roche,
573 Cat#11836145001) using a Bioruptor sonicator for 5 rounds of 1 min with 1 min off in between
574 each cycle. Lysates were centrifuged at 20,000 rpm for 15 mins at 4C and supernatants collected.
575 Lysates or conditioned media were diluted 1:1 (150 uL: 150 uL) in 50 mM Tris. 50μL of 20mM
576 MnCl2 was added to each tube, and samples were incubated for 30 mins at 37C with gentle
577 shaking. L-Histidine diluted in culture media was used as a positive control. 100μL of 50mM L-
578 Carnosine in Tris was then added to each sample, followed by incubation at 37C for 120 min with
579 gentle shaking. Finally, 500 μL of 10% trichloroacetic acid in 50 mM Tris was added to each
580 sample. Samples were centrifuged at 3000 rpm for 10 mins to remove precipitated proteins.
581 100μL of each supernatant was transferred to fresh 5 mL conical tubes. In a dark chemical hood,
582 2mL 0.3N NaOH was added to each sample, followed by 400 μL of freshly made 5 mg/mL o-
583 phthaldialdehyde solution (OPA) in 2 N NaOH. Solutions were allowed to incubate at room
584 temperature for exactly 3 mins in the dark before addition of 400 μL 6M HCl, at which point
585 samples were capped and shaken vigorously for 5s each. 100 μL of each sample was transferred
586 into a well of a black bottom 96 well plate. L-Histidine diluted in culture media was used as a
587 positive control. L-Histidine fluorescence was detected using excitation wavelength of 344 λ and
588 emission wavelength of 420 λ.

589

590 **AHA integration translation assay**

591 10-230 and 12-273 BM cells expressing control or CNDP1-targeting Tet-On shRNA's. 72h
592 after doxycycline treatment initiation, cells were labeled according to recommendations from the
593 Click-iT AHA labeling kit (Invitrogen Cat, #C10102). Briefly, cells were pre-incubated in
594 methionine-free, serum-free media (Fisher Scientific with repleted glutamine, Cat#21-012-026),
595 with or without doxycycline/carnostatine/carnosine depending on group condition, with or without
596 cycloheximide (Sigma-Aldrich, Cat #C7698-5G) for 30 mins. Then, cells were labeled with AHA
597 at a 50 μM final concentration for 4 hrs. Cells were trypsinized and permeabilized in 100 μL
598 saponin-based permeabilization buffer, washed in 1 mL 1% BSA in PBS, and incubated on 500
599 μL alkyne detection reaction cocktail with 5 μM Alexa Fluor 647 Alkyne for 30 mins at room
600 temperature. After washing with 1 mL 1% BSA in PBS, cells were resuspended in 100 μL 1%
601 BSA and stained with DAPI immediately prior to FACS analysis on a BD LSR II Flow Cytometer
602 using the APC and DAPI channels to gate for singlets. AHA incorporation in place of methionine
603 was quantified as the mean fluorescence intensity in the APC channel.

604

605 **Quantitation of Reactive Oxygen Species**

606 STC cells expressing control or CNDP1-targeting Tet-On shRNA's were plated at 250,000
607 cells per well in 6-well plates with 1 ug/mL doxycycline. An additional dose of doxycycline was
608 added at 48h post plating. At 72h post-plating, cells were incubated by replacing media with 1 mL
609 fresh serum-free media containing indicated doses of Tert-butyl hydrogen peroxide (TBHP,
610 positive control, ROS-stimulating agent, Thermo Scientific, Cat#180340050) or N-Acetyl Cysteine
611 (NAC, antioxidant, Sigma-Aldrich, Cat #180340050) for 2.5 hrs. Fresh resuspensions of THBP
612 and NAC were made on the day of each experiment in deionized sterile water. Then, CellRox
613 DeepRed reagent was added to each well (excluding negative controls) at a final concentration

614 of 500nM and allowed to incubate with cells for 30 mins at 37C protected from light. Media was
615 then collected, then adherent cells were rinsed with PBS, trypsinized, and added to their
616 respective conditioned media. After centrifugation at 1200 rpm for 4 minutes, cells were
617 resuspended in 100 μL 3% BSA and kept on ice until analysis on the BS LSRII Flow Cytometer.
618 DAPI was added immediately prior to analysis to detect dead cells. Cells were analyzed on the
619 cytometer in order of treatment group, not by shRNA expression group. Only live singlet cells
620 were compared, using the Mean Fluorescence Intensity of APC channel signal to approximate
621 ROS burden.
622
623 **Copper detection**
624 20K cells were seeded in black wall clear bottom 96 well plates treated for cell culture. All
625 conditions were treated with doxycycline and/or indicated Elesclomol and carnosine doses. After
626 24 treatment, Coppersensor-1 (CS1, MedChem Express, Cat#HY-141511) was utilized at 5 μM
627 following manufacturer indications.
628
629 **RT-qPCR**
630 RNA was isolated from cells at 80% confluence in 6 well plates using the RNeasy Mini Kit
631 (Qiagen, Cat #74104) with DNase I treatment. 1 ug of RNA was subjected to reverse transcription
632 following TaqMan™ Reverse Transcription Reagents manufacturer indications (Applied
633 Biosystems, Cat #4304134). Real time quantitative PCR was performed in 384 wells by mixing
634 Applied Biosystems™ Power SYBR™ Green PCR Master Mix (Applied Biosystems, Cat
635 #4367659), forward and reverse target gene primers at 0.2 nM final concentration (See Materials
636 Table) and 100 to 150 ng of cDNA up to 15 μl final volume.
637
638 **Immunohistochemistry**

639 Immunohistochemistry was performed using mouse anti-human CNDP1 Monoclonal
640 (OTI1A5, LSBio) and Tom20 (D8T4N) Rabbit mAb (Cell Signaling Technology) on formalin fixed,
641 paraffin embedded tissues. In brief, after deparaffinization and rehydration, heat-induced epitope
642 retrieval was performed in 0.01 M citrate buffer (pH 6.0) in a 1200-W microwave oven at 100%
643 power for 20 min. Sections were then cooled in tap water for 5 min, quenched in hydrogen
644 peroxide for 30 min, washed with PBS, and incubated with blocking serum for 30 min followed by
645 each primary antibody (Ab) diluted in buffer at room temperature for 1 h and at 4 °C overnight.
646 Abs used were Tom20 (D8T4N) Rabbit mAb (Cell Signaling Technology, Cat #42406,
647 RRID:AB_2687663) and CNDP1 Mouse anti-Human Monoclonal (OTI1A5) ab (LSBio, Cat#LS-
648 C172361, RRID: AB_3676497). Slides were washed in buffer and incubated with diluted
649 biotinylated for Tom20 (Sigma-Aldrich, Cat#A0545, RRID:AB_257896) or alkaline phosphatase
650 for CNDP1 secondary antibodies for 1 h (Alkaline Phosphatase Ab mouse, LSBio, LS-C44264,
651 RRID:AB_1050644). Avidin-biotinylated horseradish peroxidase complexes diluted at 1:500 were
652 added, and complexes were visualized with diaminobenzidine for Tom20 staining or with Fast
653 Red (Abcam, Cat# ab64254) for CNDP1 following manufacturer indications. Slides were then
654 washed in distilled water, counterstained with hematoxylin, dehydrated, and mounted with
655 permanent media. Appropriate positive and negative controls were included with the study
656 sections.
657
658 **Western Blot Analysis**
659 Cells were harvested in cold RIPA lysis buffer (Pierce, Cat # 89900) supplemented with
660 protease inhibitor and protein was quantified by DC assay. Cell lysates (30 ug of protein) were
661 resolved in 4%- 12% Bis-Tris gels (Thermo Fisher Scientific, Cat#NP0321BOX) and transferred
662 to PVDF membranes using wet transfer.
663 Membranes were blocked in either 5% non-fat milk or 5% BSA in Tris-buffered saline/1%
664 Tween 20 (TBST) for 1 hour. Membranes were incubated overnight with primary antibodies (Ab)

665 diluted in 5% milk or 5% BSA TBST. Primary ab used were anti-Human CNDP1 (352216) Ab
666 (Novus Biological, Cat#MAB2489-SP, RRID: AB_3676498), PhosphoeIF2α (Ser51) Ab (Cell
667 Signaling Technology Cat#9721S, RRID: AB_330951), EIF2S1 Monoclonal Ab (EIF2-alpha)
668 (Invitrogen, Cat#AHO0802, RRID: AB_2536316), Monoclonal Anti-Vinculin Ab produced in
669 mouse (Sigma-Aldrich, Cat#V4505-100UL. RRID: AB_477617), Atf 4 (D4B8) Rabbit mAb (Cell
670 Signaling Technology, Cat#11815S, RRID: AB_2616025), Phospho-p70 S6 Kinase (Thr389)
671 (108D2) Rabbit mAb (Cell Signaling Technology, Cat#9234T, RRID:AB_2269803), p70 S6
672 Kinase Ab (Cell Signaling Technology, Cat#9202, RRID: AB_AB_331676) 4E-BP1 (53H11)
673 Rabbit mAb (Cell Signaling Technology, Cat#9644T, RRID:AB_2799054), Phospho-4E-BP1
674 (Ser65) Ab (Cell Signaling Technology, Cat#9451T, RRID: AB_330947), Hsp90 Ab (Cell Signaling
675 Technology, Cat#4874S, RRID: AB_2121214), Rabbit HRI Polyclonal Ab (MyBioSource.com,
676 Cat#MBS2538144, RRID:AB_2885168), Monoclonal Anti-beta-Actin-Peroxidase Ab produced in
677 mouse, clone AC-15, purified from hybridoma cell culture (Sigma-Aldrich, Cat#A3854-200UL,
678 RRID:AB_262011, Rabbit anti-eIF3D/EIF3S7 Ab, Affinity Purified (Bethyl Laboratories,
679 Cat#A301-758A, RRID:AB_1210970, Eif4E Mouse, Unlabeled, Clone: 87, (BDCat#610270,
680 RRID:AB_397665), eIF4G Ab (Cell Signaling Technology, Cat#2498, RRID: AB_2096025), DAP-
681 5 Ab (F-2) (Santa Cruz Technology, Cat#sc-137011, RRID:AB_2095908 Pyruvate
682 Dehydrogenase (PDH) Ab (Cell Signaling Technology, Cat#2784, RRID: AB_2162928), 2-
683 oxoglutarate dehydrogenase (OGDH) Ab (Cell Signaling Technology, Cat#26865,
684 RRID:AB_2737585), Anti-HA-Tag Rabbit Monoclonal Ab (Cell Signaling Technology, Cat
685 #C29F4, RRID:AB_10693385). Membranes were washed 3 times for 10 min in TBST and
686 incubated in secondary antibody for 1 hour in 5% milk or BSA TBST. Membranes were washed
687 3 times for 10 minutes in TBST and incubated with ECL substrate for 1 min and exposed to film
688 or BioRad chemiluminescence dock station for imaging. Antibodies for phosphorylated proteins
689 and their respective antibodies for total protein were blotted in different membranes or

690 phosphorylated antibodies were blotted first, membrane was stripped and then the total was
691 blotted. Representative housekeeping shown.
692 The following secondary antibodies were used: Goat anti-Rabbit IgG-Peroxidase (Sigma-
693 Aldrich, Cat#A0545, RRID:AB_257896), Goat anti-mouse IgG kappa-light chain (Santa Cruz
694 Technology, Cat#sc-516102, RRID:AB_2687626) 1:10,000.
695 Quantification was performed by inverting the membrane raw image, measuring the
696 integrated density of each band using the same quantification area for all bands for the
697 housekeeping bands and the protein of interest. Quantification is represented as a ratio of the
698 signal of the protein of interest and the housekeeping protein signal and finally normalized to each
699 control condition.
700
701 **Carnosine ELISA**
702 Media (see Cell Culture above) was conditioned with melanoma cells for 24-72 hours (until
703 reaching ~80% confluency) and spun at 1200 rpm for 4 minutes to remove cells and debris.
704 Carnosine ELISA was performed following manufacturer's indications (Novus Biologicals,
705 Cat#NBP2-75013).
706
707 **Metabolomics**

708 *LC-MS/MS with the hybrid metabolomics method.* Samples were subjected to an LCMS
709 analysis to detect and quantify known peaks. A metabolite extraction was carried out on each
710 sample based on a previously described method(120). The LC column was a Millipore™ ZIC-
711 pHILIC (2.1 x 150 mm, 5 µm) coupled to a Dionex Ultimate 3000™ system and the column oven
712 temperature was set to 25 °C for the gradient elution. A flow rate of 100 µL/min was used with the
713 following buffers; A) 10 mM ammonium carbonate in water, pH 9.0, and B) neat acetonitrile. The

714 gradient profile was as follows; 80-20% B (0-30 min), 20-80% B (30-31 min), 80-80% B (31-42
715 min). Injection volume was set to 2 µL for all analyses (42 min total run time per injection).

716 MS analyses were carried out by coupling the LC system to a Thermo Q Exactive HF™
717 mass spectrometer operating in heated electrospray ionization mode (HESI). Method duration
718 was 30 min with a polarity switching data-dependent Top 5 method for both positive and negative
719 modes. Spray voltage for both positive and negative modes was 3.5 kV and capillary temperature
720 was set to 320 °C with a sheath gas rate of 35, aux gas of 10, and max spray current of 100 µA.
721 The full MS scan for both polarities utilized 120,000 resolution with an AGC target of 3e6 and a
722 maximum IT of 100 ms, and the scan range was from 67-1000 m/z. Tandem MS spectra for both
723 positive and negative mode used a resolution of 15,000, AGC target of 1e5, maximum IT of 50
724 ms, isolation window of 0.4 m/z, isolation offset of 0.1 m/z, fixed first mass of 50 m/z, and 3-way
725 multiplexed normalized collision energies (nCE) of 10, 35, 80. The minimum AGC target was 1e4
726 with an intensity threshold of $2e^5$. All data were acquired in profile mode.

727 The resulting ThermoTM RAW files were converted to SQLite format using an in-house
728 python script to enable downstream peak detection and quantification. The available MS/MS
729 spectra were first searched against the NIST17 MS/MS (121), METLIN (RRID:SCR_010500)
730 (122)and respective Decoy spectral library databases using an in-house data analysis python
731 script adapted from our previously described approach for metabolite identification false discovery
732 rate control (FDR) (123,124). Metabolite peaks were extracted based on the theoretical m/z of
733 the expected ion type, e.g., [M+H]+, with a 15 part-per-million (ppm) tolerance and a ± 0.2 min
734 peak apex retention time tolerance within an initial retention time search window of ±0.5 min. For
735 all the group-wise comparisons, t-tests were performed using the Python SciPy SciPy
736 (RRID:SCR_008058), (1.5.4) (125) library to test for differences and generate statistics for the
737 downstream analyses. For the pairwise t-tests, any metabolite with a p-value < 0.01 was
738 considered significantly regulated (up- or down-) for prioritization in the subsequent analyses.

739 Heatmaps were generated by hierarchical clustering, performed based on the imputed matrix
740 values utilizing R studio (R Project for Statistical Computing (RRID:SCR_001905) and
741 Bioconductor (RRID:SCR_006442), (1.0.12). GraphPad Prism 9 (9.4.1, GraphPad Software
742 GraphPad Prism (RRID:SCR_002798).

743 *Data analysis.* Metabolite peak intensities were extracted according to a library of m/z
744 values and retention times developed with authentic standards. Intensities were extracted with an
745 in-house script with a 10 ppm tolerance for the theoretical m/z of each metabolite, and a maximum
746 30 sec retention time window.

747

748 **RNA-sequencing analysis**

749 After 72 h induction of shRNA expression with doxycycline, cells were scraped and RNA
750 was harvested using the RNeasy Mini Kit (Qiagen, Cat #74104). For RNA-seq in cells from *in vivo*
751 experiments, tissues were harvested after intracardiac injection and 7 days of doxycycline
752 treatment. Tissues were homogenized by using a mechanic/enzymatic protocol (Collagenase
753 Sigma, Cat#C2674-100MG and DNAse I, EMD Millipore, 260913-10MU) and sorted for GFP
754 positive expression with adequate controls. RNA was extracted using the abovementioned kit.
755 RNA-Seq library preps were made using the Illumina TruSeq Stranded total RNA with RiboZero
756 Gold kit on a Beckman Biomek FX instrument, using 100 ng of total RNA as input, amplified by
757 12 cycles of PCR, and run on an Illumina NovaSeq 6000. Reads were aligned and gene
758 expression compared using the Seq-n-Slide pipeline (Seq-N-Slide (RRID:SCR_021752)). Briefly,
759 FastQC v0.11.7 was used to check fastq files for poor sequencing quality; all samples had high
760 quality. Illumina adapter sequences and poor-quality bases were then trimmed using trimmomatic
761 v0.36. Trimmed sequences were mapped to mm10 using STAR v2.6.0a (RRID:SCR_004463),
762 indexed using samtools v1.9, then quantified for UCSC genes using htseq-count

763 (RRID:SCR_011867) v0.11.1. Comparative analysis between conditions was performed using
764 DESeq2 (RRID:SCR_015687) v1.24.0 with default parameters.

765

766 **Polysome Sequencing**

767 Polysome isolation was performed by separation of ribosome-bound mRNAs via sucrose
768 gradient as previously described(126). Briefly, 14X89mm Beckman Ultra-Clear centrifuge tubes
769 were loaded with 5.5 ml of 50% and 5.5 ml 15% sucrose in Polysome Lysis Buffer (PLB) [20 mM
770 Tris (pH 7.4) in Nuclease Free H2O, 10 mM NaCl, and 3 mM MgCl2 supplemented with RiboLock
771 RNase inhibitor (ThermoFisher, Cat#EO0384) and 100µg/ml cycloheximide (Sigma-Aldrich, Cat
772 #C7698-5G) and incubated at 4 °C horizontally overnight. 10-230 BM and 12-273 BM expressing
773 shNTC and shCNDP1-1,2 were pre-treated with 100 µg/ml cycloheximide (Sigma-Aldrich, Cat
774 #C7698-5G) for 15 min at 37oC, washed twice in phosphate-buffered saline (PBS) containing
775 100 µg/ml CHX, pelleted, and flash frozen (10% was separated for total RNA and protein
776 analysis). Pellets were allowed to thaw on ice and resuspended in 750 µl of PLB. After 5 min of
777 incubation on ice, 250 µl of detergent buffer (1.2% Triton, and 0.2 M sucrose in polysome isolation
778 buffer) was added. Cells were further lysed for 10 min and lysate was clarified. Equal amount of
779 clarified lysate was layered onto 15–50% sucrose gradients and sedimented at 36 000 rpm for 2 h
780 in a SW41 rotor (Beckman Coulter) at 4 °C. Gradients were collected in 12 × 750 µl fractions by
781 pumping 60% sucrose into the bottom of the gradient and collecting from the top using an ISCO
782 fraction collector while simultaneously monitoring absorbance at 254 nm. RNA was isolated by
783 extraction using TRIZOL (ThermoFisher, Cat# 15596026) as per manufacturer's instructions.
784 Light (poorly translated) polysome fractions (2–3 ribosomes) and well-translated heavy polysome
785 fractions (≥4 ribosomes) were pooled. In parallel total RNA was extracted to normalize for
786 transcriptional changes. All experiments were performed in triplicate. RNA quality and amount
787 were determined by the Agilent Technologies kit and Nanodrop. RNAseq was carried out by the

788 NYU School of Medicine Genome Technology Core using the Illumina Hi-Seq 2500 Single Read.
789 Multiple triplicate samples were pooled for 10-230 BM. PCA analysis was performed using the
790 "stats" R package (Bioconductor (RRID:SCR_006442)) and multiple individual triplicates (12-273
791 BM shCNDP11-1 and shNTC-2 bulk) were identified as outliers and removed from further
792 processing.

793 Polysome data was analyzed using RIVET (RRID:SCR_026488, a R-Shiny-based
794 tool(126). Utilizing the matched bulk and light + heavy polysome data, RIVET uses the "limma" R
795 statistical package (RRID:SCR_010943) to determine transcripts that were over or under
796 expressed in both transcription and translation. Within the RIVET app, the transcripts for both
797 shRNAs targeting CNDP1 were combined to create a "combined" sample. The differentially
798 expressed genes identified by RIVET were exported for further analysis. Using the R package
799 "enrichplot," GSEA (Gene Set Enrichment Analysis (RRID:SCR_003199)) analyses were
800 performed on the differentially expressed gene lists to identify associated pathways possibly
801 affected by the changed genes.

802

803 **Proteomics workflow**

804 *Protein isolation*. 10-230BM cells expressing shNTC, shCNDP1-1, or shCNDP1-2 were
805 seeded at 1e6 cells per 15cm plate in triplicate and incubated in DMEM + 10% dialyzed serum +
806 1 ug/mL doxycycline for 72 hrs. STCs at ~80% confluence were scraped from 10 cm plates on
807 ice, washed once with cold PBS, and scraped in 1mL additional cold PBS into an eppendorf tube.
808 After centrifugation at 1200 rpm for 4 minutes, pellets were flash-frozen in liquid nitrogen. Upon
809 thawing, pellets were lysed in cold RIPA buffer supplemented with protease inhibitor, for 15
810 minutes with vortexing every 5 minutes. Protein concentration was determined using Micro BCA
811 Protein Assay Kit (Thermo Scientific, Cat #23235).

812 *Sample preparation for mass spectrometry analysis.* 150 µg of each protein lysate were
813 proteolytically digested and subjected to quantitative mass spectrometry on an Orbitrap Fusion
814 Lumos mass spectrometer using isobar tandem mass tags (TMT). Samples were prepared using
815 the filter-aided sample preparation (FASP) method. Briefly, each sample was reduced with DTT
816 (final concentration of 20 mM) at 57°C for 1 hour and loaded onto a MicroCon 30-kDa centrifugal
817 filter unit (Millipore) pre- equilibrated with 200 µl of FASP buffer [8 M urea and 0.1 M tris-HCl (pH
818 7.8)]. Following three washes with FASP buffer, lysates were alkylated on a filter with 50 mM
819 iodoacetamide for 45 min in the dark. Filter-bound lysates were washed three times each with
820 FASP buffer followed by 100 mM ammonium bicarbonate (pH 7.8). The samples were digested
821 overnight at room temperature with trypsin (Promega) at a 1:100 ratio of enzyme to protein.
822 Peptides were eluted twice with 100 µl of 0.5 M NaCl. The tryptic peptides were subsequently
823 desalted using an UltraMicro Spin Column, C18 (Harvard Apparatus) and concentrated in a
824 SpeedVac concentrator.

825 *TMT labeling.* The dried peptide mixture was re-suspended in 100 µl of 100 mM
826 Triethylammonium bicarbonate (TEAB) (pH 8.5). Each sample was labeled with TMT reagent
827 according to the manufacturer's protocol. In brief, each TMT reagent vial (0.8 mg) was dissolved
828 in 41 µL of anhydrous ethanol and was added to each sample. The reaction was allowed to
829 proceed for 60 min at room temperature and then quenched using 8 µL of 5% (w/v)
830 hydroxylamine. The samples were combined at a 1:1 ratio and the pooled sample was
831 subsequently desalted using strong-cation exchange and strong-anion exchange solid- phase
832 extraction columns (Strata, Phenomenex) as described.

833 *Global Proteome Analysis.* A 500 µg aliquot of the pooled sample was fractionated using
834 basic pH reverse-phase HPLC (as described) 250. Briefly, the sample was loaded onto a 4.6 mm
835 × 250 mm Xbridge C18 column (Waters, 3.5 µm bead size) using an Agilent 1260 Infinity Bio-inert
836 HPLC and separated over a 90 min linear gradient from 10 to 50% solvent B at a flow rate of 0.5
837 ml/min (Buffer A = 10 mM ammonium formate, pH 10.0; Buffer B = 90% ACN, 10 mM ammonium

838 formate, pH 10.0). A total of 120 fractions were collected and non-concatenated fractions
839 combined into 40 final fractions. The final fractions were concentrated in the SpeedVac and stored
840 at -80°C until further analysis.

841 *LC-MS/MS analysis.* An aliquot of each final fraction was loaded onto a trap column
842 (Acclaim® PepMap 100 pre-column, 75 µm × 2 cm, C18, 3, 100 Å, Thermo Scientific) connected
843 to an analytical column (EASY-Spray column, 50 m × 75 µm ID, PepMap RSLC C18, 2 µm, 100
844 Å, Thermo Scientific) using Easy nLC 1000 (Thermo Scientific) with solvent A consisting of 2% in
845 0.5% acetic acid and solvent B consisting of 80% acetonitrile in 0.5% acetic acid. The peptide
846 mixture was gradient eluted into the Orbitrap Lumos Fusion mass spectrometer (Thermo
847 Scientific) using the following gradient: 5%-23% solvent B in 100 min, 23% - 34% solvent B in 20
848 min, 34% - 56% solvent B in 10 min, followed by 56%- 100% solvent B for 20 min. Full scans
849 were acquired with a resolution of 60,000 (@ m/z 200), a target value of 4e5 and a maximum ion
850 time of 50 ms. After each full scan the most intense ions above 5E4 were selected for
851 fragmentation with HCD using the "Top Speed" algorithm. The MS/MS were acquired in the
852 Orbitrap with a resolution of 60,000 (@ m/z 200), isolation window of 1.5 m/z, target value of 1e5,
853 maximum ion time of 60 ms, normalized collision energy (NCE) of 35, and dynamic exclusion of
854 30 s.

855 *Data analysis.* The MS/MS spectra were searched against the UniProt human reference
856 proteome with the Andromeda 252 search engine integrated into the MaxQuant 253 environment
857 (version 1.5.2.8) using the following settings: oxidized methionine (M), TMT-labeled N- term and
858 lysine, acetylation (protein N-term) and deamidation (asparagine and glutamine) were selected
859 as variable modifications, and carbamidomethyl (C) as fixed modifications; precursor mass
860 tolerance was set to 10 ppm; fragment mass tolerance was set to 0.01 Th. The identifications
861 were filtered using a false-discovery rate (FDR) of 0.01 using a target-decoy approach at the
862 protein and peptide level. Only unique peptides were used for quantification and only proteins
863 with at least two unique peptides were reported. Data analysis was performed using Perseus.

864 Protein levels were median centered and log2 normalized. To identify proteins differentially
865 expressed between groups, a Welch's t-test was performed.
866
867 **ChIP-seq**
868 Around $1x10^7$ 501mel cells per IP were double crosslinked in 25mM EGS (Thermo Fisher
869 Scientific, 21565) and 1% formaldehyde (Sigma Aldrich, Cat#47608). Cells were lysed in ChIP
870 lysis buffer (CLB = 10mM Tris HCl pH8, 100mM NaCl, 1mMEDTA pH8, 0.5mM EGTA pH8, 0.1%
871 Sodium Deoxycholate, 0.5% N-lauroylsarcosine, 1% Triton X-100) and sonicated with Diagenode
872 Bioruptor for 15-30 cycles (30" ON +30" OFF max intensity). H3K27ac IP was conducted using
873 5ug of Ab/IP H3K27Ac Ab (Active Motif, Cat#91193, RRID:AB_2793797) against an IgG control
874 (Cell Signaling Technology, Cat#3900, RRID:AB_1550038) prebound to ProteinA/G magnetic
875 beads (Pierce Thermo Fisher Scientific, Cat#88803). After overnight IP, beads were washed
876 twice in Wash Buffer I (WBI, 20mM Tris HCl pH7.5, 150mM NaCl, 2mM EDTA pH8, 0.1% SDS,
877 1% Triton X100), Wash Buffer II (WBII, 10mM Tris HCl pH8, 250mM LiCl, 1mM EDTA, 1% Triton
878 X100, 0.7% Sodium Deoxycholate) and TET Buffer (10mM Trist HCl pH8, 1mM EDTA, 0.2%
879 Tween20) and eluted in Elution buffer (EB, 10mM Tris HCl pH8, 300mM NaCl, 5mM EDTA pH8,
880 0.5% SDS, 10ug RNAse A, 100ug proteinase K). ChIP elutions were purified using MinElute
881 Reaction Cleanup kit (Qiagen, Cat#28204) followed by library preparation using NEBNext Ultra II
882 DNA Library Prep Kit for Illumina (NEB, Cat# E7600S) following manufacture instructions.
883 Analysis. H3K27ac and MITF fastqs (MITF fastq obtained from GSE61967) were trimmed,
884 filtered and aligned to hg38 human genome using using Trim Galore (RRID:SCR_011847),
885 FastQC (RRID:SCR_014583) and Bowtie 2 (RRID:SCR_016368) (2.4.1). Sam output files were
886 converted into bam using SAMTOOLS (RRID:SCR_002105) (1.16124) and bigwig files were
887 generated using bamcoverage (deeptools 3.5.6125). H3K27ac and MITF peaks were called using
888 MACS (RRID:SCR_013291) (2.2.9.1126) using paired-end mode. IgG served as controls. During
889 all steps, genomic regions were filtered for blacklisted regions.

890

891 **Seahorse Metabolic Analysis**

892 30 to 50 K cells were plated on a XF96 Cell Culture Microplate. The Seahorse MitoStress
893 test protocol was followed using a Seahorse XF96 instrument (Agilent). Concentrations of
894 inhibitors injected were as follows: 2uM oligomycin, 500 nM FCCP and 1 uM antimycin A and
895 rotenone (Cayman Chemical Company, Cat#11342, Cat#15218, Cat #19433, Cat#13995,
896 respectively). After the MitoStress test, cells were fixed in the plated and stained using crystal
897 violet and dissolved with Acetic Acid 15%. Absorbance was measured at 565l. Oxygen
898 consumption rate (OCR) values for every condition were normalized to final confluence.

899

900 **Glutamine tracing**

901 For ^{13}C5-Gln tracing experiments cells were plated in a six-well plate at 2.0 × 105 cells per
902 well and allowed to attach overnight in DMEM. Cells were treated as indicated in figure legends.
903 Next, cells were washed with PBS twice and cultured for 30 mins in DMEM without phenol (Gibco,
904 Cat#A1443001) supplemented with 4 mM 13C5-Gln and 10% dialyzed serum was added. The
905 tracing medium was removed and washed with PBS. Polar metabolites were collected and
906 derivatized using MOX-TBDMS (Thermo Scientific, Cat#TS-45950, Regis Technologies,
907 Cat#77377-52-7; Cat#18162-48-6, respectively) and analyzed using a labeled amino acid
908 standard as previously described 119–122.

909

910 **Animal Studies**

911 NOD/SCID/IL2yR- /- male mice (RRID:IMSR_JAX:005557) at 8-12 weeks were used for
912 *in vivo* studies involving injection of 12-273BM STC. Male athymic nude mice

913 (RRID:IMSR_JAX:002019) were used for in vivo studies involving injection of 10-230BM STC and
914 MDA-231-Brm2. Male mice were used exclusively because injection of these short-term cultures
915 into female mice results in overwhelming ovarian tumor burden that causes mice decline before
916 brain metastasis develops.

917 All experiments were conducted following protocols approved by the NYU Institutional
918 Animal Care Use Committee (IACUC) (protocol number s16-00051). Animals experiments with
919 YUMM3.2 were conducted in AAALAC approved facilities at the University of Utah. All animal
920 protocols were reviewed and approved prior to experimentation by the Institutional Animal Care
921 and Use Committee (IACUC) at the University of Utah.

922 *Metastasis in the YUMM3.2 syngeneic model*. C57BL/6J (RRID:MGI:3028467) male and
923 female mice were housed in cages containing up to five animals of the same sex and maintained
924 at room temperature. Mice were fed a combination of Teklad Global 2920X and Teklad 3980X
925 (Inotiv), supplemented with DietGel76A and HydroGel (Clear H2O) post-weaning. One-week
926 post-weaning, mice were transitioned to Teklad Global 2920X.

927 *In vivo metastasis assays.* 100,000 cells suspended in 100 μl of PBS were injected with
928 ultrasound guidance (Visualsonics Vevo 770 Ultrasound Imaging System) into the left ventricle of
929 mice anesthetized with isoflurane. Mice were monitored weekly for metastatic progression by in
930 vivo Bioluminescence imaging (BLI). Upon weight loss > 20% of their maximum weight over the
931 course of the experiment, and/or signs of distress (neurological signs, abnormal locomotion) in
932 any experimental mice, experimental endpoint was established. At experimental endpoint, all
933 mice in all experimental groups were euthanized with ketamine/xylazine (see “Perfusion”).

934 Generally, 12 mice per group underwent intracardiac injection with cancer cells. Figure
935 legends indicate where group size may vary due to unattended death or failed intracardiac
936 injection.

937 *In vivo syngeneic allografts.* Seven to nine weeks-old glowing head mice were
938 subcutaneously injected into the dorsal area near the scapula with $5x10^4$ Yumm3.2 BrafV600E
939 Cdkn2a-/- Pten-/- cell expressing Cndp1-HA and Akt1E17K GFP-Luciferase in Matrigel and
940 observed for tumor growth. Tumors were visualized and measured weekly using bioluminescence
941 imaging (BLI), and tumor burden was quantified using bioluminescent photon output values and
942 digital caliper measurements up to 2000 mm^3. The following formulas was used to calculate tumor
943 volume: (Length X $Width^2$)/2.

944 *In-vivo BLI*. 10 minutes prior to imaging, luciferin substrate (150 mg/kg) was administered
945 to mice by intraperitoneal injection. Mice were anesthetized with isoflurane (Covetrus, Cat#11695-
946 6777-2) and imaged by IVIS Illumina instrument (PerkinElmer, (RRID:SCR_025239)) for an
947 automatically-determined duration (1-120 sec). Signal was quantified by measurement of total
948 luminescent flux (p/sec/cm2/sr) in drawn brain and body regions of interest using Living Image
949 software. For the Yumm3.2 syngeneic model organ visualization, at euthanasia, the primary tumor
950 as well as lungs, livers and brains were imaged ex vivo using the IVIS Spectrum to confirm
951 luciferase expression and to detect metastases. Living image software (version 4.5.2) was used
952 to compile images.

953 *Perfusion.* Mice were anesthetized with a ketamine (100 mg/kg, Covetrus Cat#071069)
954 and xylazine (10 mg/kg, Anased, Cat#NDC59399-110-20) cocktail by intraperitoneal injection.
955 The heart was exposed by gross dissection and an incision was made in the right atrium.
956 Subsequently, 10 mL of PBS followed by 10 mL of 4% PFA was injected into the left ventricle.

957 *Continuous shRNA-mediated gene silencing.* Starting two days prior to intracardiac
958 injection and continuing through the experimental duration, doxycycline hyclate (200 mg/kg/day)
959 was administered to mice in food pellets.

960 *Induction of gene silencing in growing metastases.* Protocol for *in vivo* metastasis assay
961 (as described above) was performed. Mice were administered standard chow at the beginning of
962 the experiment. 14-17 days (indicated in figure legend) after intracardiac injection of cancer cells,

963 gene silencing was induced by administration of doxycycline hyclate (200 mg/kg/day) in food
964 pellets.

965 *Mouse tissue processing*. Organs harvested from PFA-perfused mice were fixed in 10%
966 formalin for 72 hours, followed by several washes PBS and resuspension in 70% ethanol for 24
967 hours. Prior to embedding, brains were sectioned grossly into thirds coronally and livers were
968 sectioned by lobe. Organs were embedded in paraffin and cut into 5 μM thick sections. The
969 embedded brain thirds were sectioned coronally through the entire length of tissue at an interval
970 of 50 μM. For livers, sections were obtained from two levels 100 μM apart. For brain, sections
971 were obtained from 2 evenly spaced levels of the embedded coronal thirds. In total, this resulted
972 in 6 serial coronal brain section levels for metastatic quantification. All sections were stained with
973 H&E.

974

975 **Statistical Analysis**

976 Statistical analyses were performed with Prism 9 (RRID:SCR_002798), specific tests are
977 indicated in figure legends. Unless otherwise stated, values are averages and error bars are +/-
978 standard deviation.

979

980 **Resource Availability**

981 **Lead contact**

982 Further information and requests for resources and reagents should be directed to and will be
983 fulfilled by the lead contact, Eva Hernando (eva.hernando-monge@nyulangone.org).

984 **Material availability**

985 Requests for resources and reagents should be directed to and will be fulfilled by the lead contact,
986 Eva Hernando (eva.hernando-monge@nyulangone.org)

987 **Data and code availability**

988 RNA-sequencing/Proteomics/Metabolomics data have been deposited at [TBD] as
989 [Database:TBD] and are publicly available as of the date of publication. Additional dataset utilized
990 are detailed indicated in references, figure legends and Methods.
991 De-Identified human data is available in Supplementary Tables. They are publicly available as of
992 the date of publication until [TBD].
993 Original western blots images are available as supplementary information in Document S1.
994 All code and packages are available in this paper's methods
995 Any additional information required to reanalyze the data reported in this paper is available from
996 the lead contact upon request. Eva Hernando (eva.hernando-monge@nyulangone.org).
997

998 **Acknowledgements.** We thank the NYU Grossman School of Medicine core facilities, funded by
999 Cancer Center Support Grant (NCI/NIH; 5P30CA016087), including the Preclinical Imaging
1000 Laboratory (Youssef Zaim-Wadghiri, Orlando Aristizabal) , the Experimental Pathology Research
1001 Laboratory (Director, Dr. Cindy Loomis) for tissue processing and histology, the Proteomics Core
1002 (Director, Dr. Beatrix Ueberheide) for mass spectrometry data, Metabolomics Core (Director, Dr.
1003 Drew Jones) for metabolic profiling, Genomics Technology Center (Director, Adriana Heguy) for
1004 transcriptomics. This work was funded by NIH/NCI U54 CA263001, R21CA286244,
1005 5R01CA277425, the V Foundation, and the Melanoma Research Alliance. I.O was supported by
1006 NIH Melanoma SPORE grant NCI P50 CA225450. M.L. was funded by the University Research
1007 Priority Program (URPP). A.K was supported by T32CA009161 and T32GM136573. V.O-V was
1008 supported by 5F31CA250364. P.B. has been funded by a National Cancer Center fellowship and
1009 a Melanoma Research Alliance fellowship. S.L.H. is funded by NIH R01CA121118 and the
1010 Melanoma Research Alliance. D.E.B is funded by the NCI Predoctoral to Postdoctoral Fellow
1011 Transition Award (F99/K00) K99 CA245822-07. Uta Mackensen designed and performed the
1012 illustrations that can be found in Figure S7.

1013 **Authors contributions**

A.K., M.A.G-M and E.H conceived and designed the study. M.A.G-M, A.K., M.N., V.O-V., O.K., P.B., A. P.M and E.V.S-dM performed experiments. M.A.G-M., A.K., M.N., A.W., P.B., Y.W., M.I., X.K., S.T. and D.E.B analyzed experimental or genomic data. D.E.B., M.P., R.P., R.J.S., S.L.H., C.T.V., K.V.R. contributed to data interpretation. I.O., M.L, E.dS and B.I. provided patients tissues and/or data. A.K., M.A.G-M., D.E.B. interpreted the data. M.A.G-M, A.K., and E.H. wrote the manuscript. All authors read and approved the manuscript.

Declaration of interest

The authors declare no competing interests.

References

1. Steeg PS. Targeting metastasis. Nat Rev Cancer. 2016;16:201–18.
2. Zemek RM, Anagnostou V, Pires da Silva I, Long G V., Lesterhuis WJ. Exploiting temporal aspects of cancer immunotherapy. Nat Rev Cancer. 2024;24:480–97.
3. Soave A, Kluwe L, Yu H, Rink M, Gild P, Vetterlein MW, et al. Copy number variations in primary tumor, serum and lymph node metastasis of bladder cancer patients treated with radical cystectomy. Sci Rep. 2020;10:21562.
4. Gui P, Bivona TG. Evolution of metastasis: new tools and insights. Trends Cancer [Internet]. 2022;8:98–109. Available from: http://www.ncbi.nlm.nih.gov/pubmed/34872888
5. Karras P, Bordeu I, Pozniak J, Nowosad A, Pazzi C, Van Raemdonck N, et al. A cellular hierarchy in melanoma uncouples growth and metastasis. Nature. 2022;610:190–8.
6. Gerstberger S, Jiang Q, Ganesh K. Metastasis. Cell. 2023;186:1564–79.
7. Bergers G, Fendt S-M. The metabolism of cancer cells during metastasis. Nat Rev Cancer. 2021;21:162–80.
8. Di Martino JS, Nobre AR, Mondal C, Taha I, Farias EF, Fertig EJ, et al. A tumor-derived type III collagen-rich ECM niche regulates tumor cell dormancy. Nat Cancer. 2021;3:90–107.
9. Achrol AS, Rennert RC, Anders C, Soffietti R, Ahluwalia MS, Nayak L, et al. Brain metastases. Nat Rev Dis Primers [Internet]. 2019;5:5. Available from: http://www.ncbi.nlm.nih.gov/pubmed/30655533
10. Berghoff AS, Schur S, Füreder LM, Gatterbauer B, Dieckmann K, Widhalm G, et al. Descriptive statistical analysis of a real life cohort of 2419 patients with brain metastases of solid cancers. ESMO Open. 2016;1:e000024.
11. Schouten LJ, Rutten J, Huveneers HAM, Twijnstra A. Incidence of brain metastases in a cohort of patients with carcinoma of the breast, colon, kidney, and lung and melanoma. Cancer. 2002;94:2698–705.

1049 12. Lamba N, Wen PY, Aizer AA. Epidemiology of brain metastases and leptomeningeal
1050 disease. Neuro Oncol. 2021;23:1447–56.
1051 13. Long G V., Atkinson V, Lo S, Guminski AD, Sandhu SK, Brown MP, et al. Five-year
1052 overall survival from the anti-PD1 brain collaboration (ABC Study): Randomized phase 2
1053 study of nivolumab (nivo) or nivo+ipilimumab (ipi) in patients (pts) with melanoma brain
1054 metastases (mets). Journal of Clinical Oncology. 2021;39:9508–9508.
1055 14. Tawbi HA, Forsyth PA, Hodi FS, Algazi AP, Hamid O, Lao CD, et al. Long-term outcomes
1056 of patients with active melanoma brain metastases treated with combination nivolumab
1057 plus ipilimumab (CheckMate 204): final results of an open-label, multicentre, phase 2
1058 study. Lancet Oncol. 2021;22:1692–704.
1059 15. Long G V, Atkinson V, Lo SN, Guminski AD, Sandhu SK, Brown MP, et al. Ipilimumab
1060 plus nivolumab versus nivolumab alone in patients with melanoma brain metastases
1061 (ABC): 7-year follow-up of a multicentre, open-label, randomised, phase 2 study. Lancet
1062 Oncol. 2025;
1063 16. Rauschenberg R, Bruns J, Brütting J, Daubner D, Lohaus F, Zimmer L, et al. Impact of
1064 radiation, systemic therapy and treatment sequencing on survival of patients with
1065 melanoma brain metastases. Eur J Cancer. 2019;110:11–20.
1066 17. Vosoughi E, Lee JM, Miller JR, Nosrati M, Minor DR, Abendroth R, et al. Survival and
1067 clinical outcomes of patients with melanoma brain metastasis in the era of checkpoint
1068 inhibitors and targeted therapies. BMC Cancer. 2018;18:490.
1069 18. Tio M, Wang X, Carlino MS, Shivalingam B, Fogarty GB, Guminski AD, et al. Survival and
1070 prognostic factors for patients with melanoma brain metastases in the era of modern
1071 systemic therapy. Pigment Cell Melanoma Res [Internet]. 2018;31:509–15. Available
1072 from: http://www.ncbi.nlm.nih.gov/pubmed/29277979
1073 19. Bander ED, Yuan M, Carnevale JA, Reiner AS, Panageas KS, Postow MA, et al.
1074 Melanoma brain metastasis presentation, treatment, and outcomes in the age of targeted
1075 and immunotherapies. Cancer. 2021;127:2062–73.
1076 20. Knisely JPS, Yu JB, Flanigan J, Sznol M, Kluger HM, Chiang VLS. Radiosurgery for
1077 melanoma brain metastases in the ipilimumab era and the possibility of longer survival. J
1078 Neurosurg. 2012;117:227–33.
1079 21. Fukumura K, Malgulwar PB, Fischer GM, Hu X, Mao X, Song X, et al. Multi-omic
1080 molecular profiling reveals potentially targetable abnormalities shared across multiple
1081 histologies of brain metastasis. Acta Neuropathol. 2021;141:303–21.
1082 22. Biermann J, Melms JC, Amin AD, Wang Y, Caprio LA, Karz A, et al. Dissecting the
1083 treatment-naive ecosystem of human melanoma brain metastasis. Cell [Internet].
1084 2022;185:2591-2608.e30. Available from: http://www.ncbi.nlm.nih.gov/pubmed/35803246
1085 23. Ngo B, Kim E, Osorio-Vasquez V, Doll S, Bustraan S, Liang RJ, et al. Limited
1086 Environmental Serine and Glycine Confer Brain Metastasis Sensitivity to PHGDH
1087 Inhibition. Cancer Discov. 2020;10:1352–73.
1088 24. Karz A, Dimitrova M, Kleffman K, Alvarez-Breckenridge C, Atkins MB, Boire A, et al.
1089 Melanoma central nervous system metastases: An update to approaches, challenges,
1090 and opportunities. Pigment Cell Melanoma Res. 2022;35:554–72.

1091 25. Kleffman K, Levinson G, Rose IVL, Blumenberg LM, Shadaloey SAA, Dhabaria A, et al.
1092 Melanoma-Secreted Amyloid Beta Suppresses Neuroinflammation and Promotes Brain
1093 Metastasis. Cancer Discov. 2022;12:1314–35.
1094 26. Fischer GM, Jalali A, Kircher DA, Lee W-C, McQuade JL, Haydu LE, et al. Molecular
1095 Profiling Reveals Unique Immune and Metabolic Features of Melanoma Brain
1096 Metastases. Cancer Discov [Internet]. 2019;9:628–45. Available from:
1097 http://www.ncbi.nlm.nih.gov/pubmed/30787016
1098 27. Burdette SC, Lippard SJ. Meeting of the minds: Metalloneurochemistry. Proceedings of
1099 the National Academy of Sciences. 2003;100:3605–10.
1100 28. Piskounova E, Agathocleous M, Murphy MM, Hu Z, Huddlestun SE, Zhao Z, et al.
1101 Oxidative stress inhibits distant metastasis by human melanoma cells. Nature.
1102 2015;527:186–91.
1103 29. Nease LA, Church KP, Delclaux I, Murakami S, Astorkia M, Zerhouni M, et al.
1104 Selenocysteine tRNA methylation promotes oxidative stress resistance in melanoma
1105 metastasis. Nat Cancer. 2024;
1106 30. Chi Y, Remsik J, Kiseliovas V, Derderian C, Sener U, Alghader M, et al. Cancer cells
1107 deploy lipocalin-2 to collect limiting iron in leptomeningeal metastasis. Science (1979)
1108 [Internet]. 2020;369:276–82. Available from:
1109 https://www.science.org/doi/10.1126/science.aaz2193
1110 31. Pegova A, Abe H, Boldyrev A. Hydrolysis of carnosine and related compounds by
1111 mammalian carnosinases. Comp Biochem Physiol B Biochem Mol Biol. 2000;127:443–6.
1112 32. Jackson MC, Kucera CM, Lenney JF. Purification and properties of human serum
1113 carnosinase. Clinica Chimica Acta. 1991;196:193–205.
1114 33. Teufel M, Saudek V, Ledig J-P, Bernhardt A, Boularand S, Carreau A, et al. Sequence
1115 Identification and Characterization of Human Carnosinase and a Closely Related Non-
1116 specific Dipeptidase. Journal of Biological Chemistry. 2003;278:6521–31.
1117 34. Regazzoni L. State of the Art in the Development of Human Serum Carnosinase
1118 Inhibitors. Molecules. 2024;29:2488.
1119 35. Reddy VP, Garrett MR, Perry G, Smith MA. Carnosine: A Versatile Antioxidant and
1120 Antiglycating Agent. Science of Aging Knowledge Environment. 2005;2005.
1121 36. Peters V, Yard B, Schmitt CP. Carnosine and Diabetic Nephropathy. Curr Med Chem.
1122 2020;27:1801–12.
1123 37. Bauer K. Carnosine and Homocarnosine, the Forgotten, Enigmatic Peptides of the Brain.
1124 Neurochem Res. 2005;30:1339–45.
1125 38. Berezhnoy DS, Stvolinsky SL, Lopachev A V., Devyatov AA, Lopacheva OM, Kulikova
1126 OI, et al. Carnosine as an effective neuroprotector in brain pathology and potential
1127 neuromodulator in normal conditions. Amino Acids. 2019;51:139–50.
1128 39. Naletova I, Greco V, Sciuto S, Attanasio F, Rizzarelli E. Ionophore Ability of Carnosine
1129 and Its Trehalose Conjugate Assists Copper Signal in Triggering Brain-Derived
1130 Neurotrophic Factor and Vascular Endothelial Growth Factor Activation In Vitro. Int J Mol
1131 Sci [Internet]. 2021;22:13504. Available from: https://www.mdpi.com/1422-
1132 0067/22/24/13504
1133 40. Bellia F, Lanza V, Naletova I, Tomasello B, Ciaffaglione V, Greco V, et al. Copper(II)
1134 Complexes with Carnosine Conjugates of Hyaluronic Acids at Different Dipeptide Loading

1135 Percentages Behave as Multiple SOD Mimics and Stimulate Nrf2 Translocation and
1136 Antioxidant Response in In Vitro Inflammatory Model. Antioxidants. 2023;12:1632.
1137 41. Anderson EJ, Vistoli G, Katunga LA, Funai K, Regazzoni L, Monroe TB, et al. A
1138 carnosine analog mitigates metabolic disorders of obesity by reducing carbonyl stress.
1139 Journal of Clinical Investigation. 2018;128:5280–93.
1140 42. Prokopieva VD, Yarygina EG, Bokhan NA, Ivanova SA. Use of Carnosine for Oxidative
1141 Stress Reduction in Different Pathologies. Oxid Med Cell Longev. 2016;2016:1–8.
1142 43. Caruso G, Di Pietro L, Cardaci V, Maugeri S, Caraci F. The therapeutic potential of
1143 carnosine: Focus on cellular and molecular mechanisms. Current Research in
1144 Pharmacology and Drug Discovery. 2023;4:100153.
1145 44. Gaunitz F, Hipkiss AR. Carnosine and cancer: a perspective. Amino Acids. 2012;43:135–
1146 42.
1147 45. Renner C, Zemitzsch N, Fuchs B, Geiger KD, Hermes M, Hengstler J, et al. Carnosine
1148 retards tumor growth in vivo in an NIH3T3-HER2/neu mouse model. Mol Cancer.
1149 2010;9:2.
1150 46. Teufel M, Saudek V, Ledig J-P, Bernhardt A, Boularand S, Carreau A, et al. Sequence
1151 Identification and Characterization of Human Carnosinase and a Closely Related Non-
1152 specific Dipeptidase. Journal of Biological Chemistry. 2003;278:6521–31.
1153 47. Biermann J, Melms JC, Amin AD, Wang Y, Caprio LA, Karz A, et al. Dissecting the
1154 treatment-naive ecosystem of human melanoma brain metastasis. Cell [Internet].
1155 2022;185:2591-2608.e30. Available from: http://www.ncbi.nlm.nih.gov/pubmed/35803246
1156 48. Goding CR. Mitf from neural crest to melanoma: signal transduction and transcription in
1157 the melanocyte lineage. Genes Dev. 2000;14:1712–28.
1158 49. De Marchis S, Cosimo Melcangi R, Modena C, Ilaria Cavaretta, Peretto P, Agresti C, et
1159 al. Identification of the glial cell types containing carnosine-related peptides in the rat
1160 brain. Neurosci Lett. 1997;237:37–40.
1161 50. Karz A, Coudray N, Bayraktar E, Galbraith K, Jour G, Shadaloey AAS, et al. MetFinder: a
1162 neural network-based tool for automated quantitation of metastatic burden in histological
1163 sections from animal models. bioRxiv [Internet]. 2023;2023.09.07.555360. Available from:
1164 http://biorxiv.org/content/early/2023/09/08/2023.09.07.555360.abstract
1165 51. Meeth K, Wang JX, Micevic G, Damsky W, Bosenberg MW. The YUMM lines: a series of
1166 congenic mouse melanoma cell lines with defined genetic alterations. Pigment Cell
1167 Melanoma Res. 2016;29:590–7.
1168 52. Almazan J, Turapov T, Kircher DA, Stanley KA, Culver K, Medellin AP, et al. Combined
1169 inhibition of focal adhesion kinase and RAF/MEK elicits synergistic inhibition of
1170 melanoma growth and reduces metastases. Cell Rep Med. 2025;6:101943.
1171 53. Parkman GL, Turapov T, Kircher DA, Burnett WJ, Stehn CM, O'Toole K, et al. Genetic
1172 Silencing of AKT Induces Melanoma Cell Death via mTOR Suppression. Mol Cancer
1173 Ther. 2024;23:301–15.
1174 54. Mooyaart AL, Zutinic A, Bakker SJL, Grootendorst DC, Kleefstra N, van Valkengoed IGM,
1175 et al. Association Between *CNDP1* Genotype and Diabetic Nephropathy Is Sex Specific.
1176 Diabetes. 2010;59:1555–9.
1177 55. Iacobini C, Menini S, Blasetti Fantauzzi C, Pesce CM, Giaccari A, Salomone E, et al. FL-
1178 926-16, a novel bioavailable carnosinase-resistant carnosine derivative, prevents onset

1179 and stops progression of diabetic nephropathy in *db* / *db* mice. Br J Pharmacol.
1180 2018;175:53–66.
1181 56. Pang Z, Chong J, Zhou G, de Lima Morais DA, Chang L, Barrette M, et al. MetaboAnalyst
1182 5.0: narrowing the gap between raw spectra and functional insights. Nucleic Acids Res.
1183 2021;49:W388–96.
1184 57. Falletta P, Sanchez-del-Campo L, Chauhan J, Effern M, Kenyon A, Kershaw CJ, et al.
1185 Translation reprogramming is an evolutionarily conserved driver of phenotypic plasticity
1186 and therapeutic resistance in melanoma. Genes Dev. 2017;31:18–33.
1187 58. Rabouw HH, Langereis MA, Anand AA, Visser LJ, de Groot RJ, Walter P, et al. Small
1188 molecule ISRIB suppresses the integrated stress response within a defined window of
1189 activation. Proceedings of the National Academy of Sciences. 2019;116:2097–102.
1190 59. Schneider-Poetsch T, Ju J, Eyler DE, Dang Y, Bhat S, Merrick WC, et al. Inhibition of
1191 eukaryotic translation elongation by cycloheximide and lactimidomycin. Nat Chem Biol.
1192 2010;6:209–17.
1193 60. Musa J, Orth MF, Dallmayer M, Baldauf M, Pardo C, Rotblat B, et al. Eukaryotic initiation
1194 factor 4E-binding protein 1 (4E-BP1): a master regulator of mRNA translation involved in
1195 tumorigenesis. Oncogene. 2016;35:4675–88.
1196 61. Saxton RA, Sabatini DM. mTOR Signaling in Growth, Metabolism, and Disease. Cell.
1197 2017;168:960–76.
1198 62. Ericksen RE, Han W. Malignant manipulaTORs of metabolism: suppressing BCAA
1199 catabolism to enhance mTORC1 activity. Mol Cell Oncol. 2019;6:1585171.
1200 63. Vanweert F, Schrauwen P, Phielix E. Role of branched-chain amino acid metabolism in
1201 the pathogenesis of obesity and type 2 diabetes-related metabolic disturbances BCAA
1202 metabolism in type 2 diabetes. Nutr Diabetes. 2022;12:35.
1203 64. Shah M, Su D, Scheliga JS, Pluskal T, Boronat S, Motamedchaboki K, et al. A Transcript-
1204 Specific eIF3 Complex Mediates Global Translational Control of Energy Metabolism. Cell
1205 Rep. 2016;16:1891–902.
1206 65. Ma S, Liu J-Y, Zhang J-T. eIF3d: A driver of noncanonical cap–dependent translation of
1207 specific mRNAs and a trigger of biological/pathological processes. Journal of Biological
1208 Chemistry. 2023;299:104658.
1209 66. Mukhopadhyay S, Encarnación-Rosado J, Lin EY, Sohn ASW, Zhang H, Mancias JD, et
1210 al. Autophagy supports mitochondrial metabolism through the regulation of iron
1211 homeostasis in pancreatic cancer. Sci Adv. 2023;9.
1212 67. Schleiff E, Turnbull JL. Functional and Structural Properties of the Mitochondrial Outer
1213 Membrane Receptor Tom20. Biochemistry. 1998;37:13043–51.
1214 68. Zhang J, Ahn WS, Gameiro PA, Keibler MA, Zhang Z, Stephanopoulos G. 13C Isotope-
1215 Assisted Methods for Quantifying Glutamine Metabolism in Cancer Cells. 2014. page
1216 369–89.
1217 69. Naletova I, Greco V, Sciuto S, Attanasio F, Rizzarelli E. Ionophore Ability of Carnosine
1218 and Its Trehalose Conjugate Assists Copper Signal in Triggering Brain-Derived
1219 Neurotrophic Factor and Vascular Endothelial Growth Factor Activation In Vitro. Int J Mol
1220 Sci. 2021;22:13504.
1221 70. Barca A, Ippati S, Urso E, Vetrugno C, Storelli C, Maffia M, et al. Carnosine modulates
1222 the Sp1-Slc31a1/Ctr1 copper-sensing system and influences copper homeostasis in

1223 murine CNS-derived cells. American Journal of Physiology-Cell Physiology.
1224 2019;316:C235–45.
1225 71. Zheng P, Zhou C, Lu L, Liu B, Ding Y. Elesclomol: a copper ionophore targeting
1226 mitochondrial metabolism for cancer therapy. Journal of Experimental & Clinical Cancer
1227 Research. 2022;41:271.
1228 72. Li S-R, Bu L-L, Cai L. Cuproptosis: lipoylated TCA cycle proteins-mediated novel cell
1229 death pathway. Signal Transduct Target Ther [Internet]. 2022;7:158. Available from:
1230 https://www.nature.com/articles/s41392-022-01014-x
1231 73. Du J, Huang Z, Li Y, Ren X, Zhou C, Liu R, et al. Copper exerts cytotoxicity through
1232 inhibition of iron-sulfur cluster biogenesis on ISCA1/ISCA2/ISCU assembly proteins. Free
1233 Radic Biol Med. 2023;204:359–73.
1234 74. Vo TTT, Peng T-Y, Nguyen TH, Bui TNH, Wang C-S, Lee W-J, et al. The crosstalk
1235 between copper-induced oxidative stress and cuproptosis: a novel potential anticancer
1236 paradigm. Cell Communication and Signaling. 2024;22:353.
1237 75. Karras P, Bordeu I, Pozniak J, Nowosad A, Pazzi C, Van Raemdonck N, et al. A cellular
1238 hierarchy in melanoma uncouples growth and metastasis. Nature. 2022;610:190–8.
1239 76. Pozniak J, Pedri D, Landeloos E, Van Herck Y, Antoranz A, Vanwynsberghe L, et al. A
1240 TCF4-dependent gene regulatory network confers resistance to immunotherapy in
1241 melanoma. Cell. 2024;187:166-183.e25.
1242 77. Brady DC, Crowe MS, Greenberg DN, Counter CM. Copper Chelation Inhibits
1243 BRAFV600E-Driven Melanomagenesis and Counters Resistance to BRAFV600E and
1244 MEK1/2 Inhibitors. Cancer Res. 2017;77:6240–52.
1245 78. Sundstrøm T, Prestegarden L, Azuaje F, Aasen SN, Røsland GV, Varughese JK, et al.
1246 Inhibition of mitochondrial respiration prevents BRAF-mutant melanoma brain metastasis.
1247 Acta Neuropathol Commun. 2019;7:55.
1248 79. Chrzan N, Hartman ML. Copper in melanoma: At the crossroad of protumorigenic and
1249 anticancer roles. Redox Biol. 2025;81:103552.
1250 80. Tsherniak A, Vazquez F, Montgomery PG, Weir BA, Kryukov G, Cowley GS, et al.
1251 Defining a Cancer Dependency Map. Cell. 2017;170:564-576.e16.
1252 81. Rihel J. Copper on the brain. Nat Chem Biol. 2018;14:638–9.
1253 82. Zeid CA, Yi L, Kaler SG. Copper Metabolism and the Liver. The Liver. Wiley; 2020. page
1254 207–14.
1255 83. Chen L, Min J, Wang F. Copper homeostasis and cuproptosis in health and disease.
1256 Signal Transduct Target Ther. 2022;7:378.
1257 84. Rokicki J, Li L, Imabayashi E, Kaneko J, Hisatsune T, Matsuda H. Daily Carnosine and
1258 Anserine Supplementation Alters Verbal Episodic Memory and Resting State Network
1259 Connectivity in Healthy Elderly Adults. Front Aging Neurosci. 2015;7.
1260 85. Masuoka N, Yoshimine C, Hori M, Tanaka M, Asada T, Abe K, et al. Effects of
1261 Anserine/Carnosine Supplementation on Mild Cognitive Impairment with APOE4.
1262 Nutrients. 2019;11:1626.
1263 86. An Y, Li S, Huang X, Chen X, Shan H, Zhang M. The Role of Copper Homeostasis in
1264 Brain Disease. Int J Mol Sci. 2022;23:13850.

87. Han S, Gim Y, Jang E-H, Hur E-M. Functions and dysfunctions of oligodendrocytes in neurodegenerative diseases. Front Cell Neurosci [Internet]. 2022;16:1083159. Available from: http://www.ncbi.nlm.nih.gov/pubmed/36605616
88. Agarwal D, Sandor C, Volpato V, Caffrey TM, Monzón-Sandoval J, Bowden R, et al. A single-cell atlas of the human substantia nigra reveals cell-specific pathways associated with neurological disorders. Nat Commun. 2020;11:4183.
89. Yan R, Zhang P, Shen S, Zeng Y, Wang T, Chen Z, et al. Carnosine regulation of intracellular pH homeostasis promotes lysosome-dependent tumor immunoevasion. Nat Immunol. 2024;25:483–95.
90. Kish SJ, Perry TL, Hansen S. Regional distribution of homocarnosine, homocarnosine-carnosine synthetase and homocarnosinase in human brain. J Neurochem. 1979;32:1629–36.
91. Perry TL, Kish SJ, Sjaastad O, Gjessing LR, Nesbakken R, Schrader H, et al. Homocarnosinosis: Increased content of homocarnosine and deficiency of homocarnosinase in brain. J Neurochem. 1979;32:1637–40.
92. Ordaz RP, Garay E, Limon A, Pérez-Samartín A, Sánchez-Gómez MV, Robles-Martínez L, et al. GABAA Receptors Expressed in Oligodendrocytes Cultured from the Neonatal Rat Contain α3 and γ1 Subunits and Present Differential Functional and Pharmacological Properties. Mol Pharmacol. 2021;99:133–46.
93. Murata Y, Colonnese MT. GABAergic interneurons excite neonatal hippocampus in vivo. Sci Adv [Internet]. 2020;6:eaba1430. Available from: http://www.ncbi.nlm.nih.gov/pubmed/32582852
94. Tzilivaki A, Tukker JJ, Maier N, Poirazi P, Sammons RP, Schmitz D. Hippocampal GABAergic interneurons and memory. Neuron [Internet]. 2023;111:3154–75. Available from: https://linkinghub.elsevier.com/retrieve/pii/S0896627323004750
95. Barron T, Yalçın B, Su M, Byun YG, Gavish A, Shamardani K, et al. GABAergic neuron-to-glioma synapses in diffuse midline gliomas. Nature. 2025;
96. Tagore M, Hergenreder E, Perlee SC, Cruz NM, Menocal L, Suresh S, et al. GABA Regulates Electrical Activity and Tumor Initiation in Melanoma. Cancer Discov. 2023;13:2270–91.
97. Pakos-Zebrucka K, Koryga I, Mnich K, Ljujic M, Samali A, Gorman AM. The integrated stress response. EMBO Rep [Internet]. 2016;17:1374–95. Available from: https://www.embopress.org/doi/10.15252/embr.201642195
98. Harding HP, Zhang Y, Zeng H, Novoa I, Lu PD, Calfon M, et al. An Integrated Stress Response Regulates Amino Acid Metabolism and Resistance to Oxidative Stress. Mol Cell. 2003;11:619–33.
99. Lines CL, McGrath MJ, Dorwart T, Conn CS. The integrated stress response in cancer progression: a force for plasticity and resistance. Front Oncol. 2023;13.
100. Ma XM, Blenis J. Molecular mechanisms of mTOR-mediated translational control. Nat Rev Mol Cell Biol. 2009;10:307–18.
101. Gorrini C, Harris IS, Mak TW. Modulation of oxidative stress as an anticancer strategy. Nat Rev Drug Discov. 2013;12:931–47.
102. Tian X, Zhang S, Zhou L, Seyhan AA, Hernandez Borrero L, Zhang Y, et al. Targeting the Integrated Stress Response in Cancer Therapy. Front Pharmacol. 2021;12.

1309 103. Anderson CP, Shen M, Eisenstein RS, Leibold EA. Mammalian iron metabolism and its
1310 control by iron regulatory proteins. Biochimica et Biophysica Acta (BBA) - Molecular Cell
1311 Research. 2012;1823:1468–83.
1312 104. Pantopoulos K. Iron Metabolism and the IRE/IRP Regulatory System: An Update. Ann N
1313 Y Acad Sci. 2004;1012:1–13.
1314 105. González M, Reyes-Jara A, Suazo M, Jo WJ, Vulpe C. Expression of copper-related
1315 genes in response to copper load. Am J Clin Nutr. 2008;88:830S-834S.
1316 106. Oc S, Eraslan S, Kirdar B. Dynamic transcriptional response of Saccharomyces
1317 cerevisiae cells to copper. Sci Rep. 2020;10:18487.
1318 107. Roy G, Antoine R, Schwartz A, Slupek S, Rivera-Millot A, Boudvillain M, et al.
1319 Posttranscriptional Regulation by Copper with a New Upstream Open Reading Frame.
1320 mBio. 2022;13.
1321 108. Seiwert N, Wecklein S, Demuth P, Hasselwander S, Kemper TA, Schwerdtle T, et al.
1322 Heme oxygenase 1 protects human colonocytes against ROS formation, oxidative DNA
1323 damage and cytotoxicity induced by heme iron, but not inorganic iron. Cell Death Dis
1324 [Internet]. 2020;11:787. Available from: https://www.nature.com/articles/s41419-020-
1325 02950-8
1326 109. Hanai J, Mammoto T, Seth P, Mori K, Karumanchi SA, Barasch J, et al. Lipocalin 2
1327 Diminishes Invasiveness and Metastasis of Ras-transformed Cells. Journal of Biological
1328 Chemistry. 2005;280:13641–7.
1329 110. Xu W-X, Zhang J, Hua Y-T, Yang S-J, Wang D-D, Tang J-H. An Integrative Pan-Cancer
1330 Analysis Revealing LCN2 as an Oncogenic Immune Protein in Tumor Microenvironment.
1331 Front Oncol. 2020;10.
1332 111. Tsvetkov P, Coy S, Petrova B, Dreishpoon M, Verma A, Abdusamad M, et al. Copper
1333 induces cell death by targeting lipoylated TCA cycle proteins. Science (1979).
1334 2022;375:1254–61.
1335 112. Kong R, Sun G. Targeting copper metabolism: a promising strategy for cancer treatment.
1336 Front Pharmacol. 2023;14.
1337 113. Cerami E, Gao J, Dogrusoz U, Gross BE, Sumer SO, Aksoy BA, et al. The cBio Cancer
1338 Genomics Portal: An Open Platform for Exploring Multidimensional Cancer Genomics
1339 Data. Cancer Discov. 2012;2:401–4.
1340 114. Li T, Fan J, Wang B, Traugh N, Chen Q, Liu JS, et al. TIMER: A Web Server for
1341 Comprehensive Analysis of Tumor-Infiltrating Immune Cells. Cancer Res. 2017;77:e108–
1342 10.
1343 115. Agrawal A, Balcı H, Hanspers K, Coort SL, Martens M, Slenter DN, et al. WikiPathways
1344 2024: next generation pathway database. Nucleic Acids Res. 2024;52:D679–89.
1345 116. Robert Jan Lebbink MM. Cloning small hairpains into lentiviral vectors .
1346 https://mcmanuslab.ucsf.edu/protocol/cloning-small-hairpins-lentiviral-vectors.
1347 117. Kircher DA, Trombetti KA, Silvis MR, Parkman GL, Fischer GM, Angel SN, et al.
1348 AKT1E17K Activates Focal Adhesion Kinase and Promotes Melanoma Brain Metastasis.
1349 Mol Cancer Res [Internet]. 2019;17:1787–800. Available from:
1350 http://www.ncbi.nlm.nih.gov/pubmed/31138602

118. de Miera EV, Friedman EB, Greenwald HS, Perle MA, Osman I. Development of five new melanoma low passage cell lines representing the clinical and genetic profile of their tumors of origin. Pigment Cell Melanoma Res. 2012;25:395–7.
119. Fontanals-Cirera B, Hasson D, Vardabasso C, Di Micco R, Agrawal P, Chowdhury A, et al. Harnessing BET Inhibitor Sensitivity Reveals AMIGO2 as a Melanoma Survival Gene. Mol Cell. 2017;68:731-744.e9.
120. Jones DR, Wu Z, Chauhan D, Anderson KC, Peng J. A nano ultra-performance liquid chromatography-high resolution mass spectrometry approach for global metabolomic profiling and case study on drug-resistant multiple myeloma. Anal Chem. 2014;86:3667–75.
121. Simón-Manso Y, Lowenthal MS, Kilpatrick LE, Sampson ML, Telu KH, Rudnick PA, et al. Metabolite profiling of a NIST Standard Reference Material for human plasma (SRM 1950): GC-MS, LC-MS, NMR, and clinical laboratory analyses, libraries, and web-based resources. Anal Chem. 2013;85:11725–31.
122. Smith CA, Maille GO, Want EJ, Qin C, Trauger SA, Brandon TR, et al. METLIN. Ther Drug Monit. 2005;27:747–51.
123. Wang X, Jones DR, Shaw TI, Cho J-H, Wang Y, Tan H, et al. Target-Decoy-Based False Discovery Rate Estimation for Large-Scale Metabolite Identification. J Proteome Res. 2018;17:2328–34.
124. Wang X, Cho J-H, Poudel S, Li Y, Jones DR, Shaw TI, et al. JUMPm: A Tool for Large-Scale Identification of Metabolites in Untargeted Metabolomics. Metabolites. 2020;10.
125. Virtanen P, Gommers R, Oliphant TE, Haberland M, Reddy T, Cournapeau D, et al. SciPy 1.0: fundamental algorithms for scientific computing in Python. Nat Methods. 2020;17:261–72.
126. Ernlund AW, Schneider RJ, Ruggles K V. RIVET: comprehensive graphic user interface for analysis and exploration of genome-wide translatomics data. BMC Genomics. 2018;19:809.
127. Fernandez CA, Rosiers C Des, Previs SF, David F, Brunengraber H. Correction of13C Mass Isotopomer Distributions for Natural Stable Isotope Abundance. Journal of Mass Spectrometry. 1996;31:255–62.
128. Parker SJ, Encarnación-Rosado J, Hollinshead KER, Hollinshead DM, Ash LJ, Rossi JAK, et al. Spontaneous hydrolysis and spurious metabolic properties of α-ketoglutarate esters. Nat Commun. 2021;12:4905.
129. Biancur DE, Paulo JA, Małachowska B, Quiles Del Rey M, Sousa CM, Wang X, et al. Compensatory metabolic networks in pancreatic cancers upon perturbation of glutamine metabolism. Nat Commun. 2017;8:15965.
130. Betancourt LH, Gil J, Sanchez A, Doma V, Kuras M, Murillo JR, et al. The Human Melanoma Proteome Atlas—Complementing the melanoma transcriptome. Clin Transl Med. 2021;11.
131. Hayashi A, Ruppo S, Heilbrun EE, Mazzoni C, Adar S, Yassour M, et al. GENI: A web server to identify gene set enrichments in tumor samples. Comput Struct Biotechnol J. 2023;21:5531–7.

132. Gao J, Aksoy BA, Dogrusoz U, Dresdner G, Gross B, Sumer SO, et al. Integrative Analysis of Complex Cancer Genomics and Clinical Profiles Using the cBioPortal. Sci Signal. 2013;6.
133. de Bruijn I, Kundra R, Mastrogiacomo B, Tran TN, Sikina L, Mazor T, et al. Analysis and Visualization of Longitudinal Genomic and Clinical Data from the AACR Project GENIE Biopharma Collaborative in cBioPortal. Cancer Res. 2023;83:3861–7.
134. Li B, Severson E, Pignon J-C, Zhao H, Li T, Novak J, et al. Comprehensive analyses of tumor immunity: implications for cancer immunotherapy. Genome Biol. 2016;17:174.
135. Varešlija D, Priedigkeit N, Fagan A, Purcell S, Cosgrove N, O'Halloran PJ, et al. Transcriptome Characterization of Matched Primary Breast and Brain Metastatic Tumors to Detect Novel Actionable Targets. JNCI: Journal of the National Cancer Institute. 2019;111:388–98.
136. Xiao L, Zhou J, Liu H, Zhou Y, Chen W, Cui W, et al. RNA Sequence Profiling Reveals Unique Immune and Metabolic Features of Breast Cancer Brain Metastases. Front Oncol. 2021;11.

1410 **Figure legends**

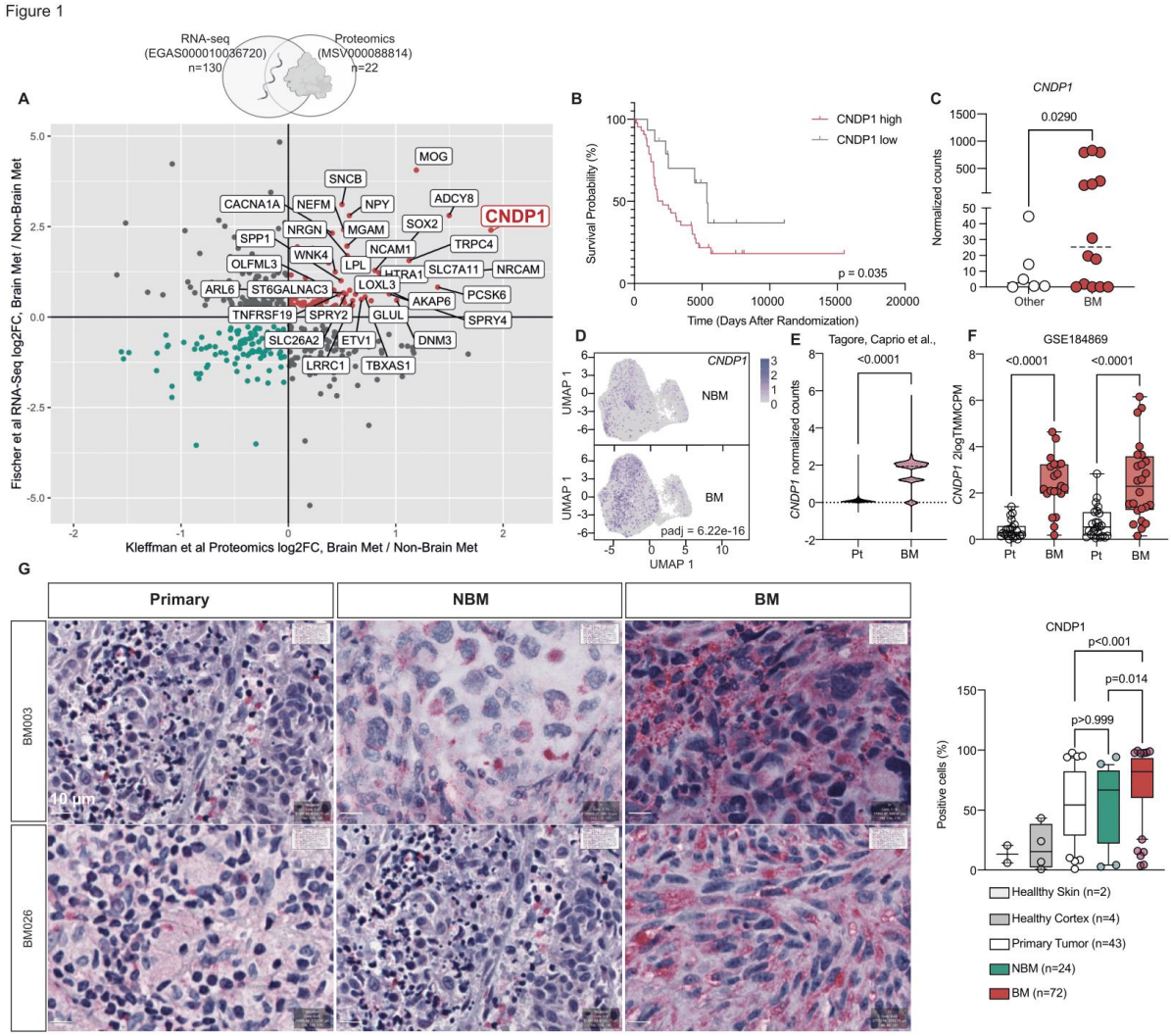

1411

1412 **Figure 1. Multi-omics approach nominates *CNDP1* as driver of melanoma brain metastasis.**

1413 **(A)** Data integration strategy showing log2Fold expression changes between patient-matched

1414 Brain Metastasis (BM) and Non-Brain Metastasis (NBM) tissue samples (RNA-sequencing n = 29

1415 patients with the following samples: 35 brain, 7 intestine, 18 lymph node, 5 lung, 12 skin.

1416 Proteomics, n = 3 patients with the following samples: 3 brain, 1 subcutaneous, 1 bowel). NBM
1417 sources in RNA-sequencing data included P value (edgeR) < 0.005 for differential expression in
1418 RNA-sequencing (EGAS000010036720, Fischer et al.) No p-value threshold was applied for
1419 proteomics data. Genes labeled are log2FC > 0.4 in both studies. Additional data can be found in
1420 Table S1 and S2.
1421 **(B)** Kaplan-Meier curve showing patient Overall Survival stratified by high and low CNDP1 protein
1422 levels in lymph nodes metastasis on MM500 study(130). Cut off established between the lower
1423 and upper quartiles of protein intensity values. T test by log-rank test. Corrected for 50% minimum
1424 tumor content.
1425 **(C)** *CNDP1* differential mRNA expression represented as normalized counts in melanoma
1426 samples spread to the lymph node that later on metastasize to the brain or to other organs.
1427 Statistical analysis by Well's t-test. Additional data can be found in Table S4.
1428 **(D)** Single Nucleus RNA-sequencing (snRNA-seq) data of human patient samples mined from
1429 Biermann et al (Series GSE185386). UMAP representing *CNDP1* expression in extracranial
1430 metastasis (NBM) vs intracranial metastasis (MBM). Statistics derived from Seurat's FindMarkers
1431 function which applies a Wilcoxon Rank Sum test.
1432 **(E)** *CNDP1* normalized counts of single cell RNA-seq data of malignant cells (n=333050 cells)
1433 from lung adenocarcinoma primary tumors (LPT) and lung adenocarcinoma brain metastasis
1434 (LBM). Data from Tagore, Caprio et al. *in press* in Nature Medicine. Statistical analysis by Welch's
1435 test.
1436 **(F)** *CNDP1* differential mRNA expression (2log TMMCPM) in breast cancer (BC) versus breast
1437 cancer brain metastasis (BCBM) paired patients' samples from indicated data set. Statistical
1438 analysis by paired t-test.
1439 **(G)** Immunohistochemistry (IHC) showing differential expression of CNDP1 in patient-matched
1440 primary, extracranial metastasis and brain metastatic samples (TMA, n samples indicated). **Left.**
1441 Representative primary, extracranial and brain metastasis IHC DAB images (BM003, BM0026)

1442 Scale=10uM**. Right.** CNDP1 expression quantification in healthy skin, healthy cortex, primary
1443 tumor, NBM (no brain metastasis) and BM (brain metastasis) samples represented as % of
1444 positive cells. P value by Paired One way ANOVA. Additional data included in Table S3.
1445 See Figure S1
1446
1447
1448
1449
1450
1451
1452
1453
1454

Figure 2

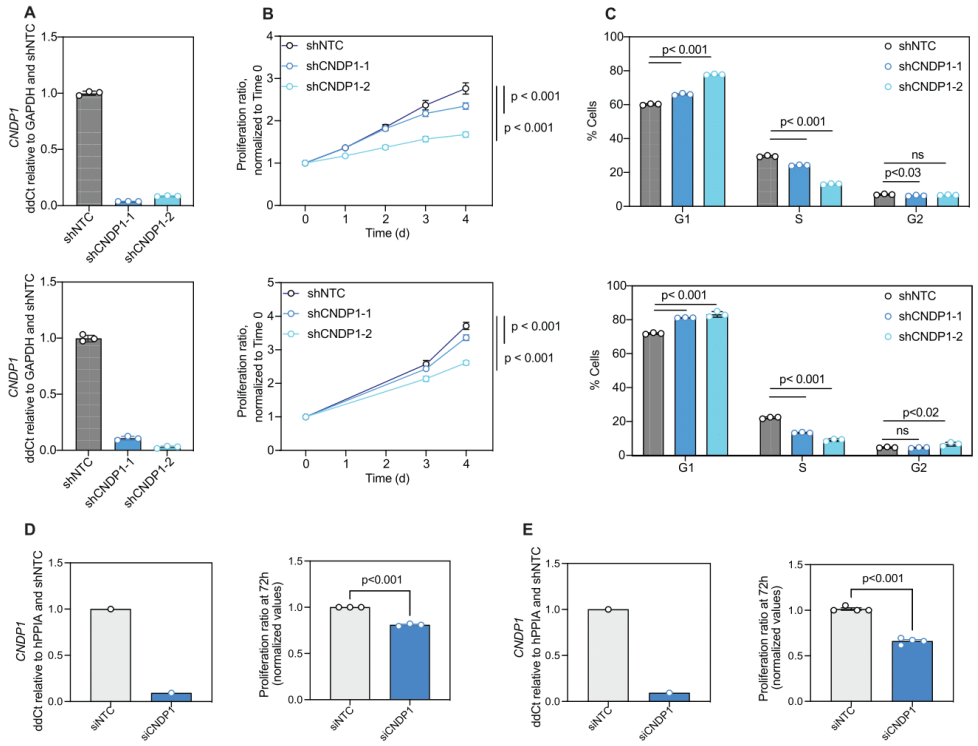

Figure 2. CNDP1 modulation impacts 2D proliferation of melanoma cells.

(A) qRT-PCR quantification of *CNDP1* mRNA, relative to GAPDH and normalized to shNTC, in 10-230 BM (top) and 12-273 (bottom) cells expressing indicated shRNA.

(B) Top. Proliferation curve performed by analyzing % confluency extracted from Incucyte image analysis normalized to day 0 of 10-230 BM cells expressing indicated tet-On shRNA (n=3, 96 h). **Bottom.** Proliferation curve performed by serial fixing and crystal violet staining of 12-273BM cells expressing indicated tet-On shRNA. Representative experiment shown of n=3 biological replicates. Statistics derived from one-way ANOVA testing between groups on the final time point.

(C) Bar plots representing % cells distributed along cell cycle phases assessed by Edu differential staining (n=2) in 10-230 and 12-273 BM cells expressing indicated tet-On shRNA. Statistical analysis by one-way ANOVA with Dunnett multiple hypothesis testing correction.

1467 **(D) Left.** qRT-PCR quantification of *CNDP1* mRNA, relative to hPPIA and then normalized to
1468 siNTC, in 10-230 BM. **Right.** Proliferation ratio of 10-230 BM cells transfected with indicated
1469 siRNAs after 72 h of culture normalized to 0h (n=3), indicated as % confluency extracted from
1470 Incucyte image analysis. Multiple biological replicates represented. Statistical analysis by one-
1471 way ANOVA.
1472 **(E). Left.** qRT-PCR quantification of *CNDP1* mRNA, relative to hPPIA and then normalized to
1473 sINTC, in 12-273 BM. **Right.** Proliferation ratio of 12-273 BM cells transfected with indicated
1474 siRNAs after 96 h culture normalized to 0h (n=4), indicated as % confluency extracted from
1475 Incucyte image analysis technology. Multiple biological replicates represented. Statistical analysis
1476 by one-way ANOVA.
1477 See Figure S2

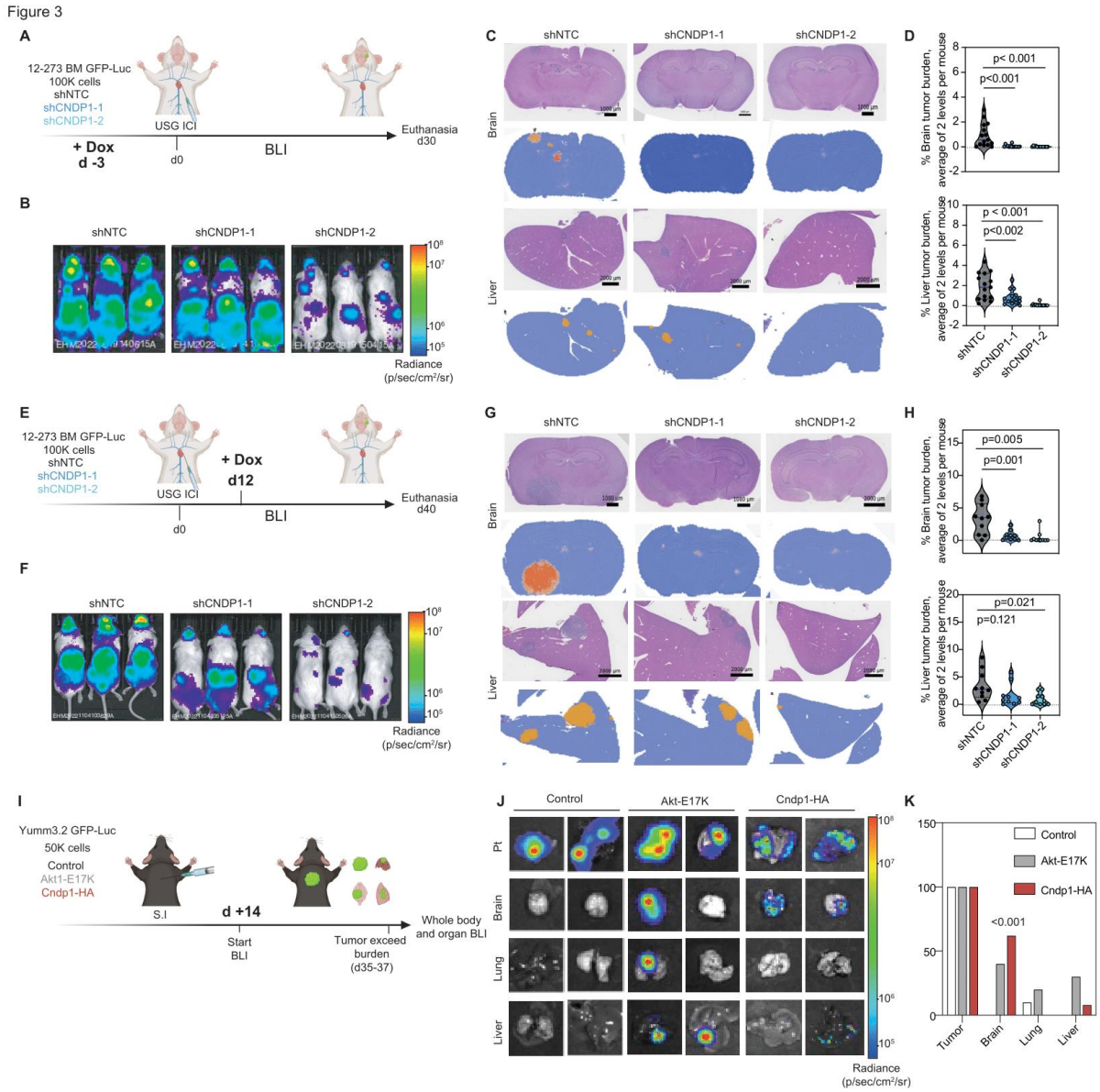

Figure 3. CNDP1 silencing impairs establishment and maintenance of *in Vivo* melanoma metastasis, and Cndp1 ectopic expression drives melanoma brain metastasis.

(A) Schematic representation of the *in vivo* xenograft constitutive approach experiment (USG ICI: Ultra Sound Guided Intra-Cardiac Injection).

(B) Representative images of whole-body *in vivo* BLI of NSG mice injected with 12-273 BM cells

1484 transduced with indicated tetON-shRNA 28 days post-injection (n = 12 mice per group, BLI
1485 represented by radiance: p/sec/cm^2/sr).
1486 **(C)** Representative H&E images and corresponding MetFinder-generated heatmaps of brain and
1487 liver sections of NSG mice injected with indicated cells (n = 12 mice per group, two sections at 3
1488 levels analyzed per organ/mice. Scale bars represent 1000 μm and 2000 μm for brain and liver,
1489 respectively).
1490 **(D)** Tumor burden in brain parenchyma, leptomeninges and liver quantified as the percent of area
1491 occupied by tumor and average of 2 levels of sectioning per organ (100 μM separation), obtained
1492 by MetFinder analysis. Statistical analysis by one-way ANOVA.
1493 **(E)** Schematic representation of the *in vivo* xenograft therapeutic approach experiment (USG ICI).
1494 **(F)** Representative images of whole-body *in vivo* BLI of NSG mice injected with 12-273 BM cells
1495 transduced with indicated tetON-shRNA at day 36 post-injection (n = 12 mice per group, BLI
1496 expressed as radiance: p/sec/cm^2/sr).
1497 **(G)** Representative H&E and MetFinder brain and liver metastasis sections of NSG mice injected
1498 with indicated vectors (n = 12 mice per group; duplicated sections and levels analyzed per
1499 organ/mice. Scale bar representative of 1000 μm and 2000 μm for brain and liver, respectively)
1500 **(H)** Tumor burden in brain parenchyma, leptomeninges and liver quantified as the percent of
1501 tumor-occupied area vs total organ area and averaged of 2 levels of sectioning per organ.
1502 Obtained by performing MetFinder analysis. Statistical analysis by one-way ANOVA.
1503 **(I)** Schematic representation of *in vivo* allograft experiment with indicated conditions. S.I:
1504 Subcutaneous injection.
1505 **(J)** Ex vivo BLI of organs in the corresponding groups of mice injected with YUMM3.2 cells control
1506 or transduced with Akt1-E17K or Cndp1-HA in indicated organs (Pt=Primary tumor). (n = 9,10
1507 &11 mice per group, respectively. BLI expressed as radiance: p/sec/cm^2/sr).
1508 **(K)** Bar graph representing % of tumor incidence for primary (Pt), brain, lung and liver metastasis

1509 in mice injected with indicated conditions. Statistical analysis results from one-way ANOVA

1510 comparing metastasis incidence at end point (1=yes, 0=no).

1511 See Figure S3

1512

1513

1514

1515

1516

1517

1518

1519

1520

1521

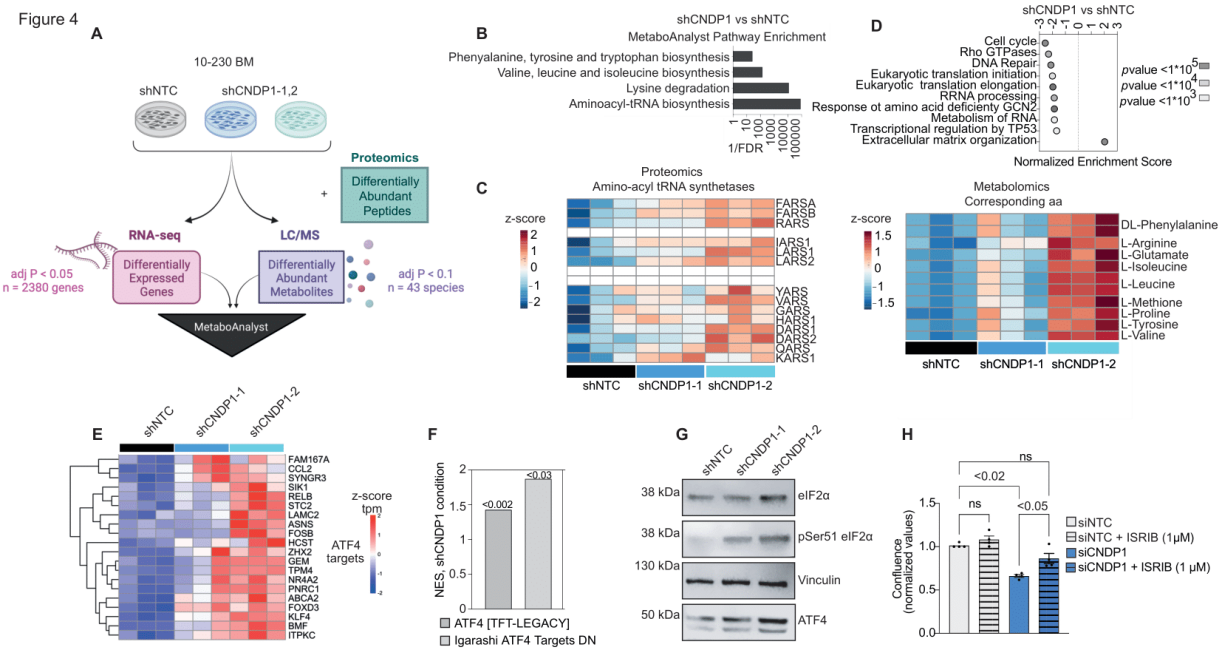

Figure 4. CNDP1 knockdown elicits an integrative stress response in melanoma cells.

(A) Workflow of RNA-sequencing and LC/MS-based nonpolar metabolomics integrative studio in 10-230BM cells transduced with indicated tetON-shRNA.

(B) Differential gene expression/metabolite abundance between shNTC vs shCNDP1-1 and shCNDP1-2 by indicated adjusted p values. MetaboAnalyst executed hypergeometric testing by combining p-values for metabolites and transcripts according to their relative proportion in each pathway. (RNA-seq: DESeq2, Metabolomics: T-test, pathways enrichment FDR < 0.05). See Tables S5-7

(C) Heatmap of t-Aminoacyl synthetases expression across different conditions paired with a heatmap of expression of their corresponding amino acids. MS/MS-based proteomics and LC/MS-based metabolomics were conducted on lysates of 10-230 BM cells expressing the indicated shRNA treated with doxycycline for 72 hours in 10% dialyzed serum DMEM.

1535 Differentially expressed proteins were identified by unpaired, two- tailed t-test comparing 2 groups
1536 normalized abundance: shCNDP1-1 and shCNDP1-2 vs shNTC (Data represented by z-score as
1537 indicated).
1538 **(D)** Integrated Gene Set Enrichment analysis (GSEA) of 12-273 and 10-230 BM shNTC vs both
1539 shCNDP1 tetON-shRNA RNA sequencing represented by Normalized Enrichment Score using
1540 Reactome Gene Ontology Analysis (RNA-seq: DESeq2, adjust p value < 0.001 and FC > 1.5).
1541 See Table S6.
1542 **(E)** Differential expression testing by DESeq2 nominated ATF4 targets in both shCNDP1 vs
1543 shNTC conditions in 10-230 BM RNA sequencing. (Data represented by z-score as indicated).
1544 **(F)** Pathway analysis via the Seq-n-Slide pipeline tested for pathway enrichment in differentially
1545 expressed genes between shCNDP1 and shNTC 10-230 BM RNA sequencing (Adjust p value
1546 indicated).
1547 **(G)** Representative immunoblots of phosphoSerine51 eIF2a, total-eIF2a, ATF4 and
1548 housekeeping (HK) protein Vinculin in lysates of 10-230 BM transduced with indicated tetON-
1549 shRNA. See Document S1 for details.
1550 **(H)** Proliferation ratio of 12-273 BM cells transfected with indicated siRNAs for CNDP1 silencing
1551 after 96 h of culture normalized to 0h (n=4), either treated with vehicle (DMSO) or ISRIB (phospho-
1552 eIF2a inhibitor, 1 uM) performed by analyzing % confluency extracted from Incucyte image
1553 analysis. Statistical analysis by one-way ANOVA. Proliferation ratio for 12-230 BM
1554 siNTC/siCNDP1 also shown in Figure 2 E.
1555 See also Figure S4
1556
1557

Figure 5

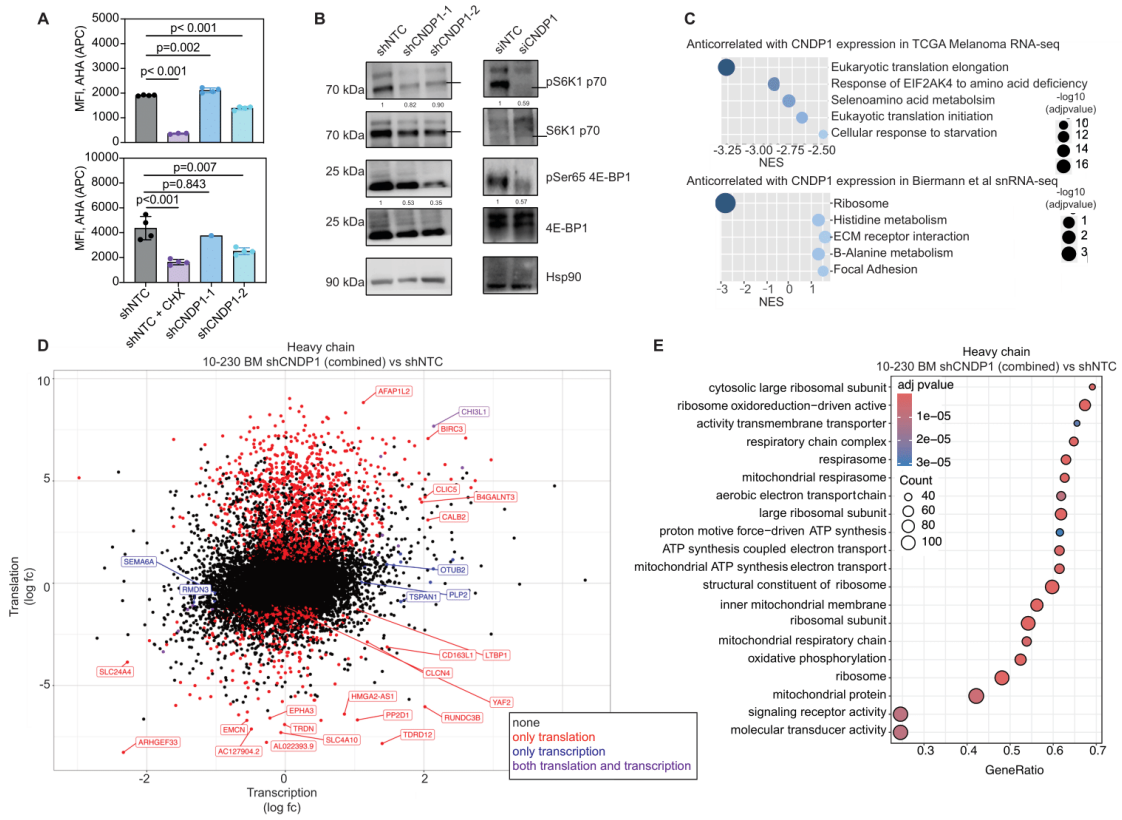

Figure 5. CNDP1 knockdown rewires translation program towards mitochondrial transcripts.

(A) 10-230 and 12-273 BM transduced with indicated tetON-shRNAs and treated with doxycycline during 72h, labeled with AHA (APC) for 4 hours and analyzed by flow cytometry. Cycloheximide (CHX, 50 ug/ml) was used as a positive control of translation shutdown. Statistics rendered by one-way ANOVA with Dunnet's multiple hypothesis testing correction.

(B) Left. Representative immunoblots of phospho-S6K1 p70 (Threonine 389), S6K1 p70, phosphoSer65 4E-BP, total 4EBP and housekeeping (HK) protein Hsp90 in lysates of 10-230 BM transduced with indicated tetON-shRNA. **Right.** Representative immunoblots of phospho-S6K1 p70 (Threonine 389), S6K1 p70, phosphoSer65 4E-BP, 4EBP and housekeeping (HK) protein Hsp90 in lysates of 10-230 BM cells transfected with siRNA NTC or CNDP1 as indicated. Band

1570 correspondent to p70 S6K1 is indicated. Results for HRI, phosphoSer51 and total eiF2α
1571 expression from same samples shown in Figure 6K and Figure S4H, respectively. Ratio of protein
1572 phosphorylation shown normalized to total protein and HK protein levels. See Document S1 for
1573 details.
1574 **(C)** GENI (gene set enrichment identifier124) was applied to TCGA melanoma samples (n = 472)
1575 using the Reactome 2022 pathway database. Five anticorrelating gene sets with FDR < 0.05 were
1576 represented.
1577 **(D)** Genes differentially expressed in shCNDP1 (combined) vs shNTC polysome heavy chain (log
1578 fc Translation vs log fc Transcription; $p<0.05$, lfc > 1) at translation, transcription and both
1579 transcription and translation levels in 10-230 BM cells. See Table 11.
1580 **(E)** Integrated Gene Enrichment analysis of Heavy Chain RNA sequencing of 10-230 BM
1581 shCNDP1 (combined) vs shNTC represented by Normalized Enrichment Score using Reactome
1582 Gene Ontology Analysis (RNA-seq: adjust p value < 0.05).
1583 See also Figure S5

Figure 6

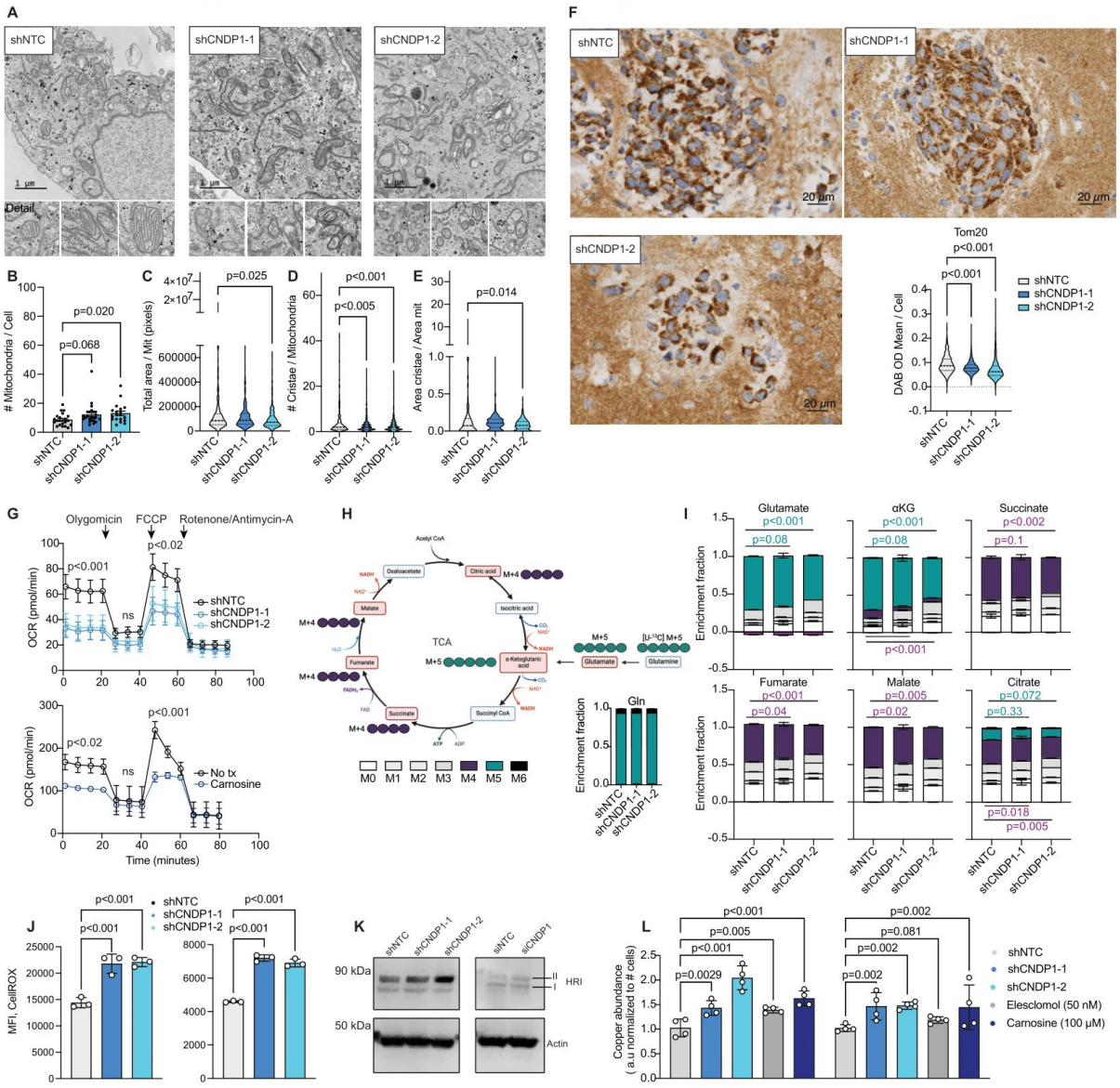

Figure 6. CNDP1 knockdown melanoma cells display profound mitochondrial defects, copper overload and ROS accumulation.

(A) Mitochondria imaging using electron microscopy of 10-230 BM transduced with indicated tetON-shRNA. Scale =1 μM.

(B-E) Quantification of number of mitochondria per cell **(B)**, mitochondria area **(C)**, cristae number

1590 per mitochondria **(D)** and cristae area per mitochondria **(E)** area in 10-230 BM. Statistical analysis
1591 by one-way ANOVA ($p<0.05$ or indicated).
1592 **(F)** Tom20 expression by IHC in BM from 12-273 BM cells transduced with indicated shRNAs
1593 induced with doxycycline during 5 days. Scale = 200 μM. Quantification of Tom20 cytosolic
1594 staining DAB intensity per cell and per mice. Statistical analysis by two-way ANOVA ($p<0.001$).
1595 **(G) Top.** Seahorse MitoStress analysis of OCR in 12-273 BM transduced with indicated tetON-
1596 shRNA. Statistical analysis by one-way ANOVA. Representative replicate shown (n=3, $p<0.05$ or
1597 indicated). **Bottom** Seahorse MitoStress analysis of OCR in 12-273 BM treated with Carnosine
1598 40 mM overnight. Statistical analysis by one-way ANOVA. Representative replicate shown (n=3,
1599 $p<0.05$ or indicated).
1600 **(H)** Schematic model of glutamine metabolism in cancer cells. Green (M+5) and purple circles
1601 (M+4) represent carbons derived from [U-13C5] glutamine. The black arrows indicate oxidative
1602 and reductive carboxylation flux from glutamine. Cells were cultured with [U-^{13}C5] glutamine for 6
1603 h before metabolite extraction and gas chromatography-mass spectrometry (GC-MS) analyses.
1604 Normalized distribution of glutamine in mentioned conditions in 12-273 BM cells transduced with
1605 indicated tetON-shRNAs treated with doxycycline for 24h are shown. (n = 3); data are shown as
1606 the mean ± SD.
1607 **(I)** Normalized distributions of glutamine, glutamate, and TCA cycle metabolites, including α-
1608 ketoglutarate (αKG), succinate, fumarate, malate and citrate, in 12-273 BM cells transduced with
1609 indicated tetON-shRNAs treated with doxycycline for 24h are shown. (n = 3); data are shown as
1610 the mean ± SD. Statistical analysis by one-way ANOVA. P value indicated.
1611 **(J)** Mean fluorescence intensity of CellROX in live cells as determined by DAPI- status in 10-230
1612 (left) and 12-273 BM (right) cells. Statistical analysis by one-way ANOVA. Representative
1613 replicate shown (n=3).
1614 **(K) Left.** Representative immunoblots of II & I HRI fractions and housekeeping (HK) protein b-

1615 actin in lysates of 12-273 BM transduced with indicated tetON-shRNA. **Right.** Representative
1616 immunoblots of II & I HRI fractions and housekeeping (HK) protein b-actin in lysates of 10-230
1617 BM cells transfected with siRNA NTC or CNDP1 as indicated. II fraction considered as the
1618 autophosphorylated. Results for translation related proteins, phosphoSer51 and total eiF2α
1619 expression from same samples shown in Figure 5B and Figure S4H, respectively. Representative
1620 HK shown. See Document S1 for details.
1621 **(L)** Copper abundance represented as ratio of emission signal at 563 nm in indicated conditions
1622 in 10-230 BM (left) and 12-273 BM (right) normalized to total number of cells quantified by crystal
1623 violet (595 nm absorbance values). Statistical analysis by one-way ANOVA. Representative
1624 replicate shown (n=3).
1625 See also Figure S6
1626
1627
1628

Figure S1

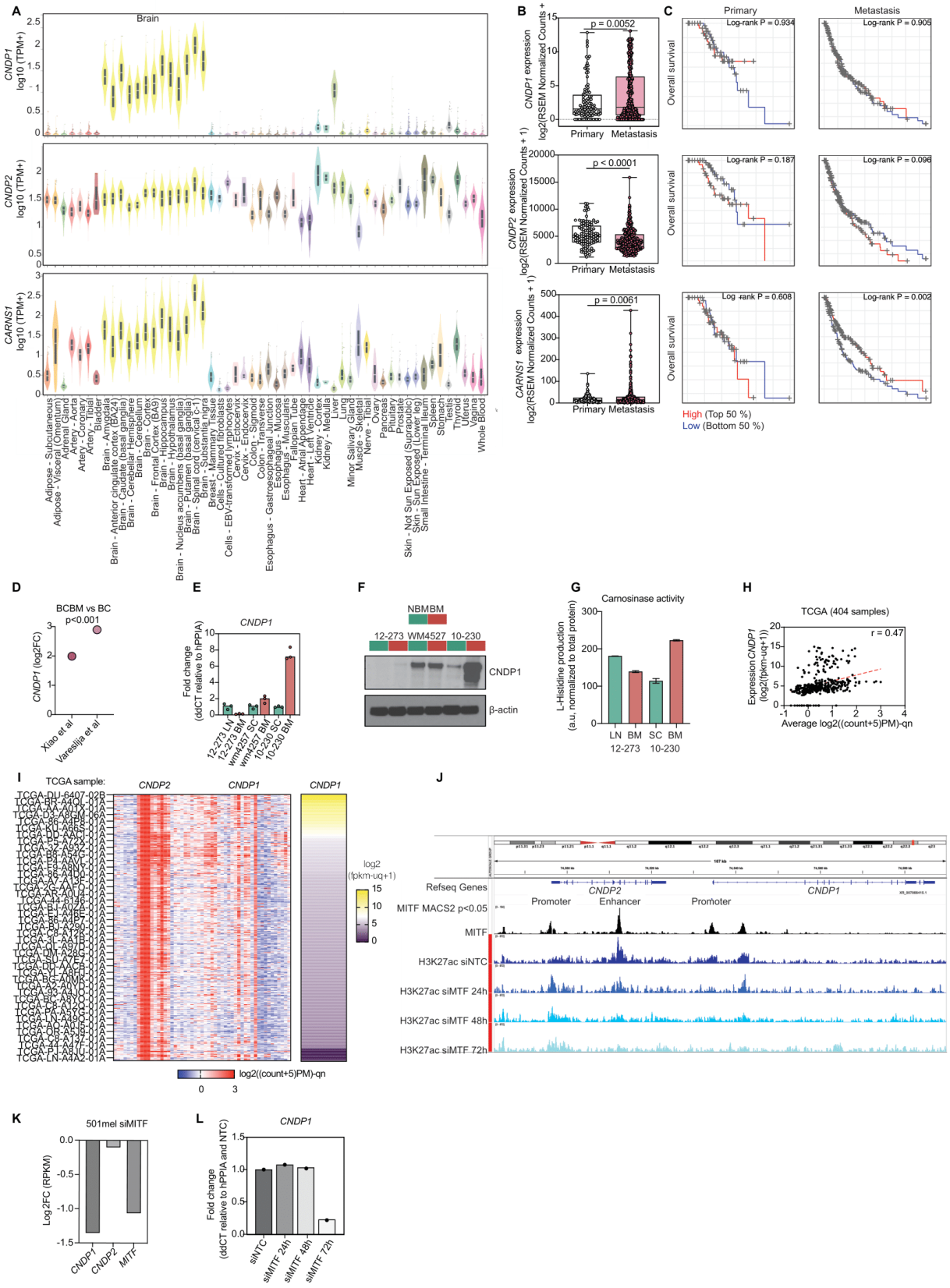
A
Brain
CNDP1 log10 (TPM+)
CNDP2 log10 (TPM+)
CARNS1 log10 (TPM+)
B
CNDP1 expression log2(RSEM Normalized Counts + 1)
p = 0.0052
CNDP2 expression log2(RSEM Normalized Counts + 1)
p < 0.0001
CARNS1 expression log2(RSEM Normalized Counts + 1)
p = 0.0061
Primary
Metastasis
C
Primary
Metastasis
Log-rank P = 0.934
Log-rank P = 0.905
Log-rank P = 0.187
Log-rank P = 0.096
Log-rank P = 0.608
Log-rank P = 0.002
Overall survival
High (Top 50 %)
Low (Bottom 50 %)
D
BCBM vs BC
p<0.001
CNDP1 (log2FC)
Xiao et al
Varesija et al
E
CNDP1
Fold change (ddCT relative to hPPIA)
12-273 LN
12-273 BM
wm4527 SC
wm4527 BM
10-230 SC
10-230 BM
F
NBMBM
12-273
WM4527
10-230
CNDP1
β-actin
G
Carnosinase activity
L-Histidine production (a.u. normalized to total protein)
LN
BM
SC
BM
12-273
10-230
H
TCGA (404 samples)
r = 0.47
Expression CNDP1 (log2(fpkm-uq+1))
Average log2((count+5)PM)-qn
I
TCGA sample:
CNDP2
CNDP1
CNDP1
log2 ((fpkm-uq+1))
log2((count+5)PM)-qn
J
Refseq Genes
CNDP2
CNDP1
Promoter
Enhancer
Promoter
MITF MACS2 p<0.05
MITF
H3K27ac siNTC
H3K27ac siMTF 24h
H3K27ac siMTF 48h
H3K27ac siMTF 72h
K
501mel siMITF
Log2FC (RPKM)
CNDP1
CNDP2
MITF
L
CNDP1
Fold change (ddCT relative to hPPIA and NTC)
siNTC
siMTF 24h
siMTF 48h
siMTF 72h

1630 **Figure S1. *CNDP1 In silico* analysis in melanoma databases. Related to Figure 1.**

1631 **(A)** Comparative analysis of log 10 transcription *CNDP1, CNDP2* and *CARNS1* expression levels
1632 (TPM+1) in human normal tissues mined from GTEx, the Genotype-Tissue Expression project.

1633 **(B)** *CNDP1, CNDP2, CARNS1* (RSEM analysis in normalized counts) expression in primary vs
1634 metastatic melanoma human samples from Melanoma dataset Cancer Genome Atlas RNA
1635 sequencing (n = 472 total samples from 469 patients. n = 369 metastases and n = 103 primary).
1636 P value by unpaired, two-tailed t-test with Welch's correction.

1637 **(C)** Kaplan-Meier curves showing patient Overall Survival stratified by high and low *CNDP1,*
1638 *CNDP2* and *CARNS1* gene expression (RNA-seq) in primary and metastatic tumor on
1639 TCGA(113,132,133) Melanoma (SKCM Firehouse Legacy, n = 472) and log-rank test by
1640 TIMER2.0(114,131,134).

1641 **(D)** 2logFC *CNDP1* expression in breast cancer data bases described in the indicated references
1642 (135,136) (adj p value $p<0.0001$).

1643 **(E)** *CNDP1* expression (qRT-PCR) in matched extracranial (NBM) and brain metastasis (BM)
1644 derived short term cultures 12-273, WM4527, 10-230. Expression represented as Fold Change
1645 relative to housekeeping gene (hPPIA) and to extracranial derived matched short-term culture
1646 (n=3). Additional data can be found in Table S1

1647 **(F)** Immunoblot showing CNDP1 expression in patient-matched extracranial (NBM) and brain
1648 metastasis (BM) derived short term cultures 12-273BM, WM-4527, 10-230BM. Additional data
1649 can be found in Table S1. See also Document S1 for details.

1650 **(G)**. L-Histidine liberation assay as carnosinase activity read-out in conditioned media of 10-230
1651 and 12-273 paired matched STC. Additional data can be found in Table S1. Two technical
1652 replicates shown.

1653 **(H)** *CNDP1* expression significantly correlates with the average epigenetic accessibility around
1654 *CNDP1* promoters. In red is shown the linear regression line. R represents the Spearman
1655 coefficient.

1656 **(I)** Combined heatmap showing the epigenetic accessibility surrounding *CNDP1* and *CNDP2* loci
1657 in a subset of TCGA patients (left) and *CNDP1* expression in the corresponding samples (right),
1658 (n=404)
1659 **(J)** IGV snapshot of MITF and the active chromatin marker H3K27ac genomic occupancy around
1660 *CNDP1* and *CNDP2* loci generated in 501mel. MITF binds to *CNDP1* promoter and H3K27ac loss
1661 upon MITF silencing at *CNDP1* promoter strongly suggests a direct MITF-dependent CNDP1
1662 regulation.
1663 **(K)** Bar plot of the mRNA expression of *CNDP1, CNDP2* and *MITF* upon MITF silencing in 501mel
1664 cell. *CNDP1* expression is strongly reduced following MITF depletion compared to *CNDP2* (data
1665 extrapolated from Laurette et al., 2015, GSE61967).
1666 **(L)** *CNDP1* expression (qRT-PCR) in 501Mel melanoma cells after 24, 48 and 72 h MITF silencing
1667 (siMITF). Expression represented as Fold Change relative to housekeeping gene (hPPIA) and
1668 non-targeting control silencing (siNTC).
1669
1670

Figure S2

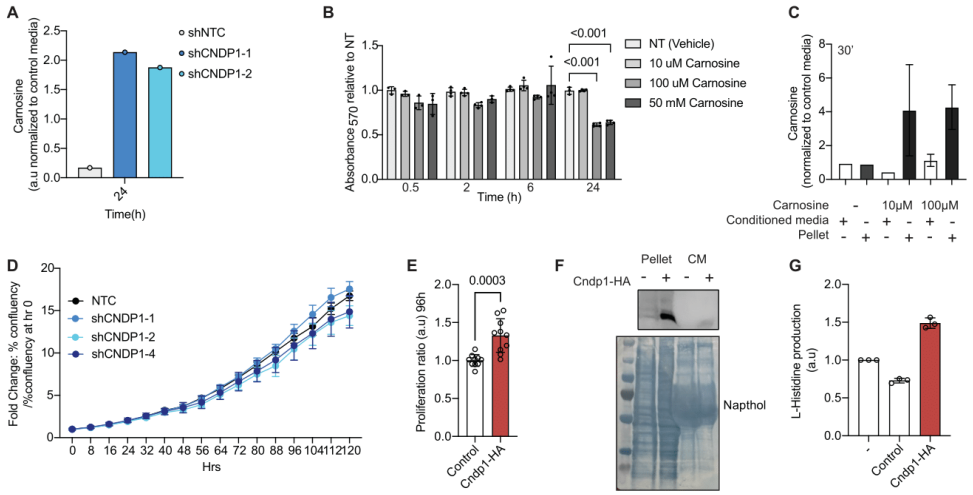

Figure S2. CNDP1 modulation effect in melanoma cells proliferation. Related to Figure 2.

(A) Carnosine accumulation measured by ELISA represented as normalized values to Carnosine concentration in shNTC conditions (30 mins under culture) in 12-273 transduced with indicated tetON-shRNAs treated with doxycycline for 24h. Mean of two technical replicates shown.

(B) Proliferation ratio of 10-230 BM cells cultured with 10 μm, 100 μm and 50 mM Carnosine concentrations during 0.5, 2, 6 and 24 h of culture normalized to not treated (NT) of their respective time points (n=3, technical replicates). Confluency obtained by treating the cells with Resazurin and measuring absorbance after 3 hours of treatment at 570 nm. Statistical analysis by one-way ANOVA.

(C) Carnosine accumulation shown as normalized units to STC media in conditioned media and pellet after 30 minutes of treatment.

(D) Proliferation ratio of SKMEL-239 cells transfected with indicated shRNAs after 96 h of culture normalized to 0h, indicated as % confluency extracted from Incucyte image analysis.

(E) Proliferation ratio performed by serial fixing and crystal violet staining of Yumm3.2 BrafV600E/wt Cdkn2a-/- Pten-/- control or ectopically expressing Cndp1-HA after 96h as

1686 indicated.

1687 **(F)** Immunoblot showing Cndp1-HA expression in conditioned media and pellets of Yumm3.2
1688 BrafV600E/wt Cdkn2a-/- Pten-/- control or ectopically expressing Cndp1-HA. See also Document
1689 S1 for details.

1690 **(G)** L-Histidine liberation assay as carnosinase activity read-out in pellets of Yumm3.2
1691 BrafV600E/wt Cdkn2a-/- Pten-/- control or ectopically expressing Cndp1-HA. Three technical
1692 replicates shown.

1693 One representative technical replicate shown for all the above assays.

Figure S3

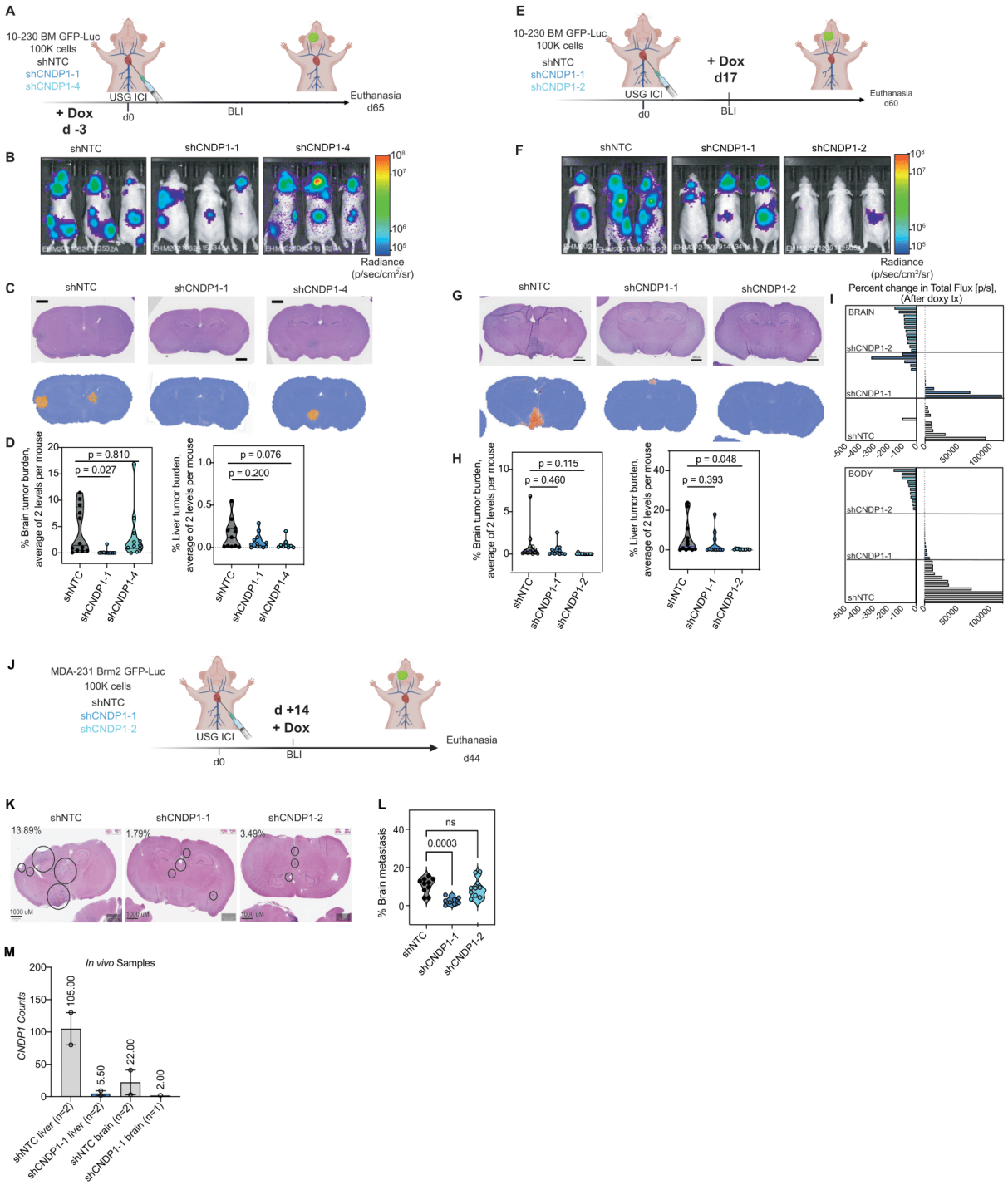

Figure S3. CNDP1 Silencing Decreases *In Vivo* Melanoma Metastasis. Related to Figure 3.

(A) Schematic representation of the *in vivo* xenograft constitutive approach experiment (USG ICI).

1697 **(B)** Representative images of whole-body *in vivo* BLI of athymic/nude mice injected with 10-230
1698 BM cells transduced with indicated tetON-shRNA 52 days post-injection (n = 12 mice per
1699 condition, BLI represented by radiance: p/sec/cm^2/sr).
1700 **(C)** Representative H&E and MetFinder brain metastasis sections of nude mice injected with
1701 indicated (n = 12 mice per condition, duplicated sections and levels analyzed per organ/mice,
1702 Scale bar 1000 μm and 2000 μm for brain and liver, respectively).
1703 **(D)** Tumor burden in brain, leptomeningeal and liver quantified as the percent of area occupied
1704 by the tumor of the total organ area and averaged of 2 levels of sectioning per organ obtained by
1705 performing MetFinder analysis. Statistical analysis by one-way ANOVA.
1706 **(E)** Schematic representation of the *in vivo* xenograft therapeutic approach experiment (USG ICI:
1707 Ultra Sound Guided Intra-Cardiac Injection).
1708 **(F)** Representative images of whole-body *in vivo* BLI of nude mice injected with 10-230 BM cells
1709 transduced with indicated tetON-shRNA day 59 post-injection (n = 12 mice per condition, BLI
1710 expressed as radiance: p/sec/cm^2/sr).
1711 **(G)** Representative H&E and MetFinder brain and liver metastasis sections of NSG mice injected
1712 with indicated (n = 12 mice per condition, duplicated sections and levels analyzed per organ/mice,
1713 Scale bar 1000 μm and 2000 μm for brain and liver, respectively).
1714 **(H)** Tumor burden in brain, leptomeningeal and liver quantified as the percent of area occupied
1715 by the tumor in the total organ area and averaged of 2 levels of sectioning per organ. Obtained
1716 by performing MetFinder analysis. Statistical analysis by one-way ANOVA.
1717 **(I)** Percent change in IVIS signal in the brain (top) and whole body (bottom) from days 12 to 36 of
1718 nude mice injected with 10-230 BM cells transduced with indicated tetON-shRNA. One bar = one
1719 mouse, n = 10 mice/group.
1720 **(J)** Schematic representation of the *in vivo* xenograft therapeutic approach experiment (USG ICI:
1721 Ultra Sound Guided Intra-Cardiac Injection).

1722 **(K)** Representative H&E images and corresponding quantitation of metastasis burden in brain
1723 sections of NSG mice injected with MDA-231 BrM2 cells transduced with indicated tetON-shRNA
1724 obtained by manual analysis. Not burden in lung, liver or kidneys detected.
1725 **(L)** Tumor burden in brain quantified as the percent of area occupied by tumor and average of
1726 two levels of sectioning per organ (100 μM separation) obtained by manual analysis (n=10, 8, and
1727 12 mice per group, two sections and two levels analyzed per organ/mice). Statistical test: one-
1728 way ANOVA. Scale bars represent 1000 μm. Not burden in lung, liver or kidneys detected.
1729 **(M)** *CNDP1* expression (counts) in RNA sequencing of 12-273 BM GFP positive cells harvested
1730 from 4 mice livers and 3 mice brains of the indicated conditions after USG ICI and 7 days of
1731 doxycycline treatment.
1732
1733
1734
1735
1736
1737
1738
1739
1740
1741

Figure S4

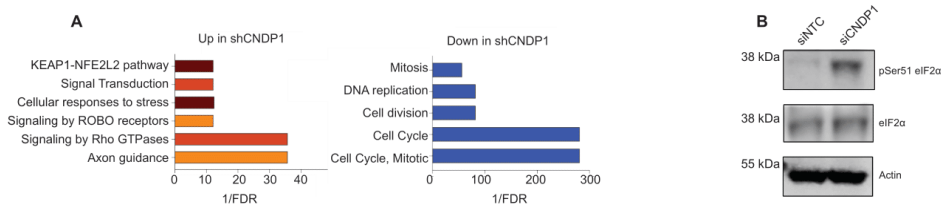

Figure S4. Proteomics changes upon CNDP1 silencing in melanoma cells. Related to Figure 4.

(A) Representation of DAVID functional annotation algorithm of upregulated (right) and downregulated (left) differentially expressed proteins identified by unpaired, two- tailed t-test comparing 2 groups: shCNDP1-1 and shCNDP1-2 versus shNTC. Represented by 1/FDR as indicated. See Table S10.

(B) Representative immunoblots of phophoSerine51 eIF2α and total eIF2α, housekeeping (HK) protein β-actin in lysates of 10-230 BM cells transfected with siRNA NTC or CNDP1 as indicated. Results for HRI and translation related proteins expression from samples shown in Figure 6K and Figure 5B, respectively. Total and phospho-proteins were blotted in different membranes. Representative HK shown. See Document S1 for details.

Figure S5

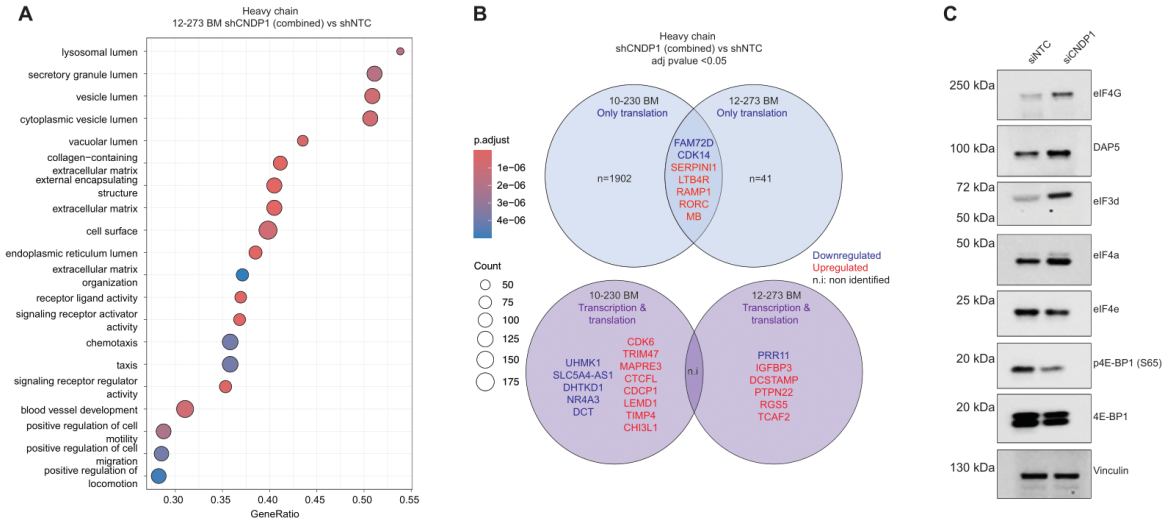

Figure S5. Extended characterization of translation phenotype of CNDP1 KD melanoma cells. Related to Figure 5.

(A) Integrated Gene Enrichment analysis of 12-273 BM heavy chain both shCNDP1 vs shNTC RNA sequencing represented by Normalized Enrichment Score using Reactome Gene Ontology Analysis (RNA-seq: adjust p value < 0.05).

(B) Venn diagram including common transcripts changing as indicated at translation level (top) and transcription and translation level (bottom) in both 10-230 and 12-273 BM shCNDP1 (combined) vs shNTC polysome heavy chain (adjusted p value <0.05, n.i - non-identified). See Table S11.

(C) Representative immunoblot of eIFs proteins and phophoSerine51 4E-BP1, 4E-BP1 and housekeeping (HK) protein Vinculin in lysates of 12-273 BM cells transfected with siRNA NTC or CNDP1 as indicated. See Document S1 for details.

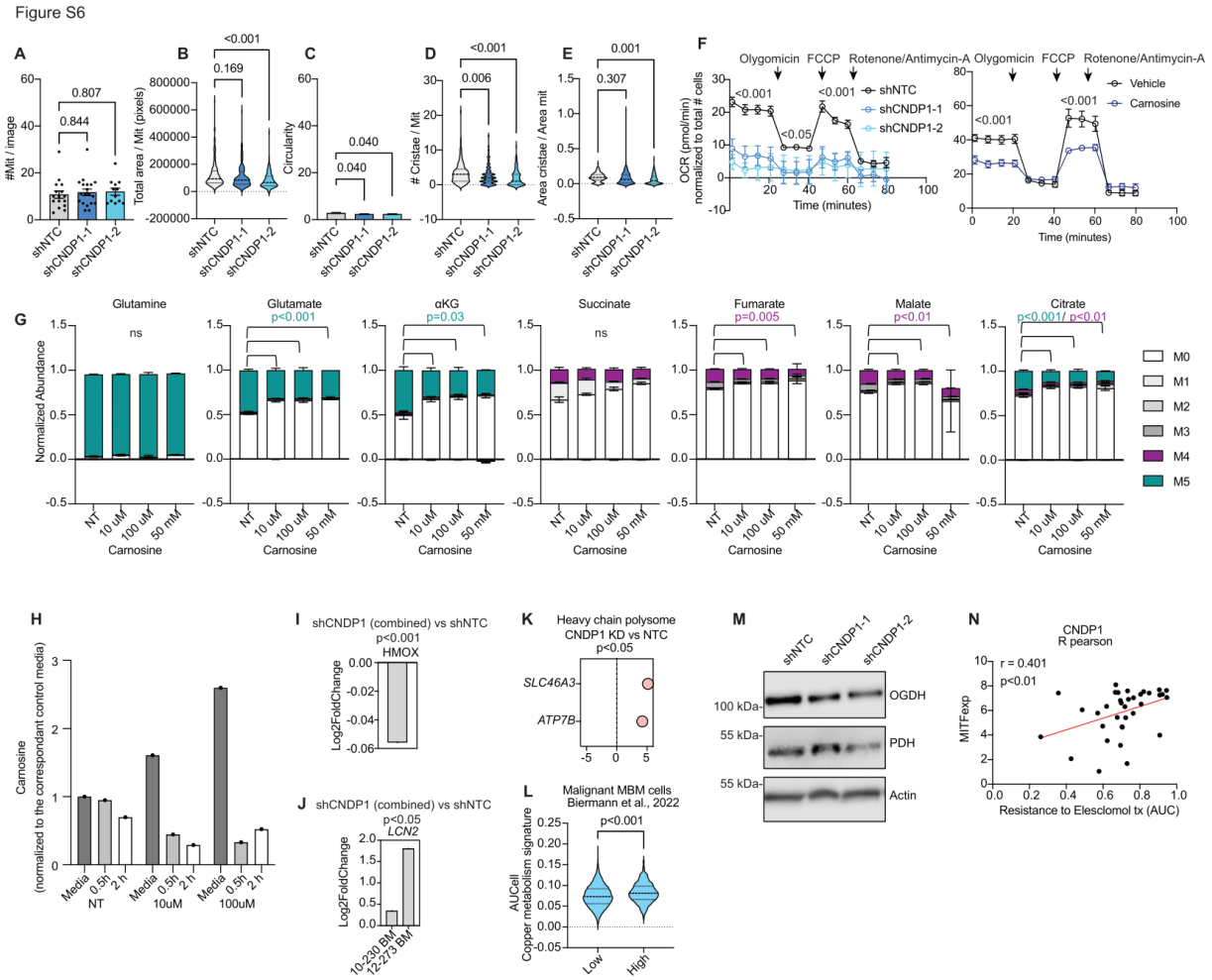

Figure S6. Extended characterization of mitochondrial phenotype of CNDP1 KD melanoma cells. Related to Figure 6.

(A-E) Quantification of total mitochondria per cell **(A)**, mitochondria area **(B)**, circularity **(C)**, cristae number per mitochondria **(D)** and cristae area per mitochondria area **(E)** in 12-273 BM. Statistical analysis by one-way ANOVA.

(F) Seahorse MitoStress analysis of OCR in 10-230 BM transduced with indicated tetON-shRNA and MDA-231 Brm2 treated as indicated. Statistical analysis by one-way ANOVA. Representative replicate shown (n=3, p<0.05 or indicated).

(G) Normalized distributions of glutamine, glutamate, and TCA cycle metabolites, including α-

1777 ketoglutarate (αKG), succinate, fumarate, malate and citrate, in 10-230 BM cells treated with 10
1778 10 μm, 100 μm and 50 mM Carnosine for 30 minutes are shown. (n = 3); data are shown as the
1779 mean ± SD. Statistical analysis by one-way ANOVA. P value indicated. Cells were cultured with
1780 [U-^{13}C5] glutamine for 6 h before metabolite extraction and gas chromatography-mass
1781 spectrometry (GC-MS) analyses.
1782 **(H)** Carnosine accumulation measured by ELISA represented as normalized values to carnosine
1783 concentration in dialyzed media supplemented with indicated concentrations in 10-230 BM cells
1784 cultured with 10 μm, 100 μm and 50 mM Carnosine concentrations during 0.5, 2 h. Mean of two
1785 technical replicates shown. Results for 0.5 h also shown in Figure S2C.
1786 **(I)** 2logFold Change of HMOX protein abundance measured by proteomics (MS/MS) in 10-230
1787 BM cells transduced with indicated tetON-shRNAs. Differentially expressed proteins identified by
1788 unpaired, two- tailed t-test comparing 2 groups: shCNDP1-1 and shCNDP1-2 versus shNTC.
1789 **(J)** 2logFoldChange of *LCN2* transcript expression of both shCNDP1 tetON-shRNA vs shNTC in
1790 10-230 BM and 12-230 BM cells. RNA sequencing data. p value < 0.05.
1791 **(K)** 2logFold Change of *ATP7B* and *SLC46A3* transcript of Heavy Chain RNA sequencing of 10-
1792 230 BM shCNDP1 vs shNTC. p value < 0.05.
1793 **(L)** AUCell (Area Under the Curve) measurement of copper homeostasis gene signature
1794 (WikiPaths, WP3286) in *CNDP1* high expression versus *CNDP1* low expression in MBM cells
1795 from Biermann et al., 2022 data mining. Statistical analysis by one-way ANOVA**,** p<0.001.
1796 **(M)** Representative immunoblots of OGDH, PDH and housekeeping (HK) protein β-actin in lysates
1797 of 10-230 BM cells transfected with indicated sh-RNAs. See document S1 for details.
1798 **(N)** R Pearson correlation between melanoma cell lines classified by their MITF expression and
1799 resistance to Elesclomol treatment expressed as AUC of cell viability after treatment. Data mining
1800 from Depmap.

Figure S7

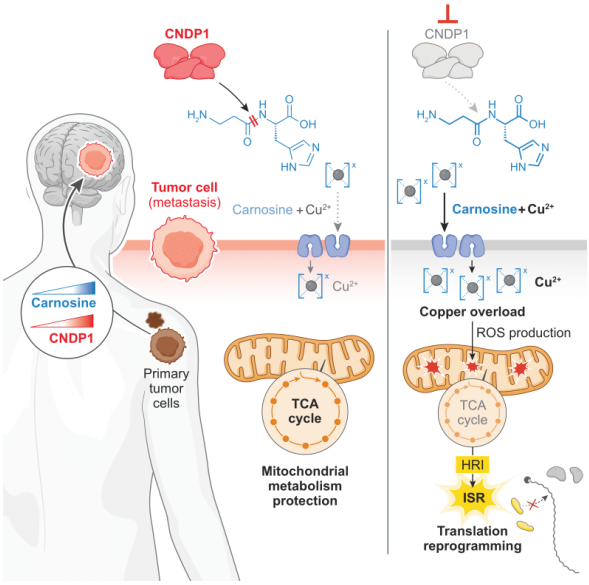

Figure S7. Graphical representation of CNDP1 role in brain metastasis.

1815 **Supplementary information.**

1816 **Document S1.** Raw western blot images

1817 **Supplementary tables.**

1818 **Table S1.** Extracranial (NBM) and Brain metastasis (BM) samples included in analysis. Related
1819 to Figure 1

1820 **Table S2.** Extracranial (NBM) and Brain metastasis (BM) samples integration results. Significantly
1821 changing candidates shown. Related to Figure 1

1822 **Table S3.** Tissue microarray codified tumor sites. Related to Figure 1

1823 **Table S4.** CNDP1 normalized counts from RNA-sequencing of melanoma extended to the lymph
1824 node. Metastasis follow up information. Related to Figure S1

1825 **Table S5.** Significantly differentially produced metabolites in CNDP1 KD (shCNDP1-1 and
1826 shCNDP1-2) vs control cells (shNTC) in 10-230 BM cells after 72 hours of doxycycline treatment
1827 (LC-MS, Hybrid Metabolomics). Related to Figure 4

1828 **Table S6.** Differentially expressed genes (DEGs) in CNDP1 KD (shCNDP1-1 and shCNDP1-2)
1829 vs control cells (shNTC) in 10-230 and 12-273 BM cells after 72 hours of doxycycline treatment
1830 (RNA-sequencing). Related to Figure 4

1831 **Table S7.** MetaboAnalyst analysis 10230 BM CNDP1 KD. Related to Figure 4

1832 **Table S8.** Differentially expressed proteins in CNDP1 KD (shCNDP1-1 and shCNDP1-2) vs
1833 control cells (shNTC) in 10-230 after 72 hours of doxycycline treatment (LC-MS/MS). Related to
1834 Figure 4

1835 **Table S9.** Gene Ontology analysis (GO) from differentially expressed genes (DEGs) in CNDP1
1836 KD (shCNDP1-1 and shCNDP1-2) vs control cells (shNTC) in 10-230 and 12-273 BM cells after
1837 72 hours of doxycycline treatment (RNA-sequencing)

1838 **Table S10.** DAVID analysis 10230 BM CNDP1 KD LC-MS/M. Related to Figure 4S

1839 **Table S11.** Differentially expressed transcripts in the heavy chain polysomes of CNDP1 KD
1840 (shCNDP1-1 and shCNDP1-2) vs control cells (shNTC) in 10-230 and 12-273 BM after 72 hours
1841 of doxycycline treatment (RNA sequencing). Related to Figure 5 and S5
1842 **Table S12.** Differential gene expression and gene ontology of CNDP1 high versus CNDP1 low
1843 expression cells from Biermann 2022. Related to Figure 5.
1844 **Materials.** All materials used in this manuscript are referenced by catalog number in this file.
1845

1846